

Shower development of particles with momenta from 1 to 10 GeV in the CALICE Scintillator-Tungsten HCAL

The CALICE Collaboration*

This note contains preliminary CALICE results, and is for the use of members of the CALICE Collaboration.

ABSTRACT: We present a study of the showers initiated by low momentum ($p \leq 10$ GeV) electrons, pions and protons in the highly granular CALICE scintillator-tungsten HCAL. The data were taken at the CERN PS in September-October 2010. The analysis includes energy resolution measurements for each particle type and studies of the longitudinal shower development. The results are compared with several GEANT4 models.

*Corresponding author: A. Lucaci-Timoce (angela.isabela.lucaci.timoce@cern.ch)

Contents

1. Introduction	2
2. Beam-line setup and trigger configuration	2
3. Calibration and temperature correction	3
4. Simulation	6
4.1 Mokka implementation	6
4.2 GEANT4 models	7
4.3 Generation and Digitization of the Simulation	9
5. Analysis of the e^-/e^+ data	11
5.1 Data selection	11
5.2 The Novosibirsk fit function	12
5.3 Systematic uncertainties	14
5.4 Electromagnetic response and energy resolution	15
5.5 Comparison with simulation	18
6. Analysis of the π^-/π^+ data	21
6.1 Calorimeter response	26
6.2 Longitudinal shower development	27
7. Analysis of the proton data	28
7.1 Calorimeter response	30
7.2 Longitudinal shower development	35
8. Summary and conclusions	37
A. List of selected runs	38
B. Cross-talk factor	39
C. Electromagnetic energy distributions and Novosibirsk fits	41
D. Comparison of methods to measure electromagnetic energy resolution	44
E. Selection of hadron events	47
F. Comparison of methods to measure hadronic energy resolution	49

1. Introduction

The Compact Linear Collider (CLIC) is an e^+e^- linear collider under study [1], aiming at center-of-mass energies up to 3 TeV. For the barrel hadronic calorimeter of experiments at CLIC, a detector with tungsten absorber plates is considered, as it provides sufficient depth to contain the high energy showers of jets while limiting the diameter of the surrounding solenoid.

In order to test such a detector in real conditions, the CALICE collaboration constructed a tungsten absorber structure, to be combined with existing readout layers of the Analog Hadronic Calorimeter (AHCAL) [2] and of the Digital HCAL (DHCAL) [3].

This paper presents results obtained with the CALICE tungsten AHCAL (W-AHCAL) prototype at the CERN PS in September-October 2010 with mixed runs containing electrons, pions and protons with a momentum range of 1 to 10 GeV¹.

The calorimeter consists of a 30 layer sandwich structure of tungsten absorber plates, and highly segmented scintillator tiles read out by wavelength shifting fibers coupled to SiPMs, with a total of 6480 channels. The prototype's dimensions are $1 \times 1 \times 0.75$ m³, amounting to 3.9 nuclear interaction lengths λ_I and to 85 radiation lengths X_0 . The high granularity of the detector is ensured by the 3×3 cm² tiles placed in the center of each active plane, surrounded by 6×6 cm² and 12×12 cm² tiles at the edges.

Detailed information about the absorber structure, as well as about the beam-line instrumentation and data taking conditions can be found in [4].

2. Beam-line setup and trigger configuration

The data presented in this note have been recorded in the secondary T9 beam line [10] of the CERN PS East Area [11]. The primary proton beam hits a target 57 m upstream the W-HCAL prototype. A momentum-selection and focusing system is used to create a mixed beam of electrons, muons, pions and protons with momenta between 1 and 10 GeV. The momentum spread $\Delta p/p$ is of the order of 1%. The beam size is chosen such that the resulting Gaussian spread in x and y at the W-AHCAL surface is approximately 3×3 cm² for 10 GeV pions.

Figure 1 shows a sketch of the beam-line instrumentation and the trigger setup. The secondary beam passes two Cherenkov counters (A and B), an external scintillator and wire chamber not connected to the CALICE DAQ, two trigger scintillators and a tracking system of three wire chambers.

The Cherenkov counters are filled with CO₂ gas with pressures adjustable up to 3.5 bar absolute. The Cherenkov information is read out digitally through photo-multiplier tubes and subsequent discriminators with a fixed threshold. The Cherenkov signals arrive in the DAQ with a delay of 45 ns with respect to the main trigger signal and are used offline for particle identification.

The information from the scintillator and wire chamber belonging to the beam-line instrumentation are used during beam tuning and not recorded for offline analysis. The two $10 \times 10 \times 1$ cm³ scintillator triggers are read out through photo-multipliers and discriminators. The standard trigger signal is built inside the CALICE DAQ as a coincidence of the two scintillator signals.

The information from three 11×11 cm² wire chambers [12] is read out through a CAEN V1290N TDC [13] and recorded for the full width of the trigger event record of 6.3 μ s. It is used

¹In this paper, the natural system of units, with $\hbar = c = 1$, is used.

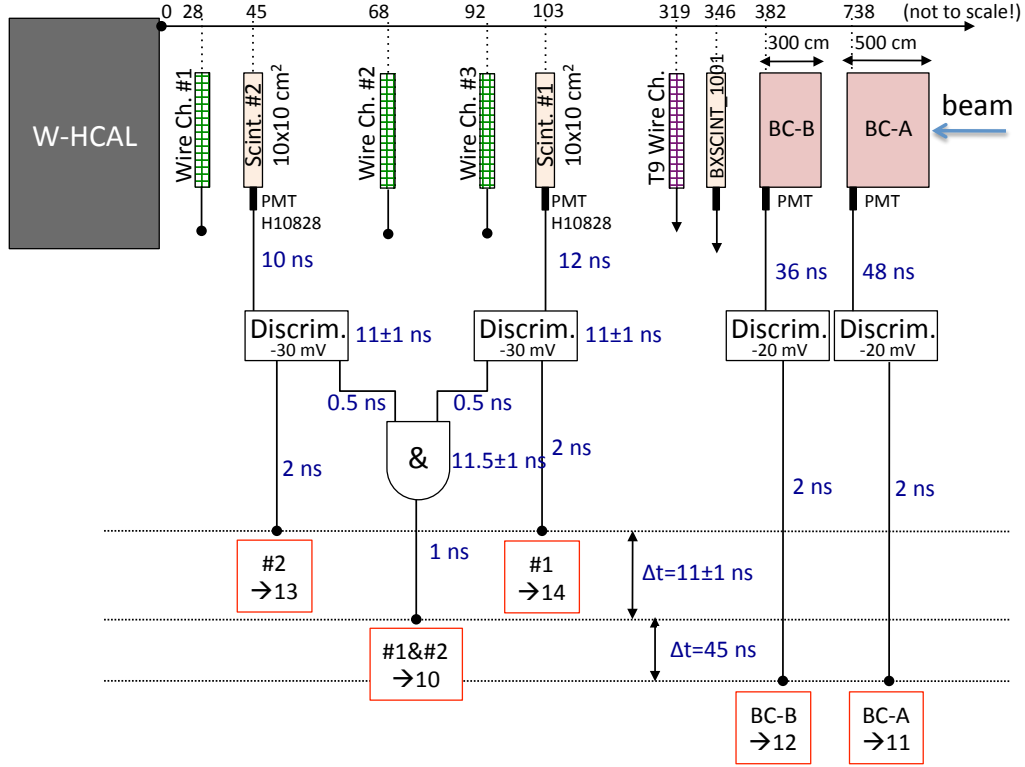


Figure 1: Sketch of the beam-line and trigger setup for the data taking in the T9 beam line of the CERN-PS.

40 offline to reconstruct the track of the incident particle and predict its position on the calorimeter
41 surface.

42 3. Calibration and temperature correction

43 The responses of all calorimeter cells are equalized to a common physics signal based on minimum
44 ionizing particles (MIPs), for which dedicated muon runs from the CERN T7 are used. Several
45 steps are necessary to translate signals measured with the SiPM readout (in ADC channels) to
46 information about the deposited energy (in MIPs).

The calibration of a single cell i is done according to:

$$E_i[\text{MIPs}] = \frac{A_i[\text{ADC}]}{A_i^{\text{MIP}}[\text{ADC}]} \cdot f_{\text{resp}}(A_i[\text{pixels}]), \quad (3.1)$$

47 where:

- 48 • $A_i[\text{ADC}]$ is the amplitude registered in cell i , in units of ADC channels;
- 49 • $A_i^{\text{MIP}}[\text{ADC}]$ is the MIP amplitude in cell i , measured also in ADC channels;
- 50 • $f_{\text{resp}}(A_i[\text{pixels}])$ is the SiPM response function which corrects for the non-linearity of the
51 SiPM response that is due to the limited number of pixels (1156) and to the finite pixel re-
52 recovery time (20-500 ns). This function acts on the amplitude expressed in number of pixels,

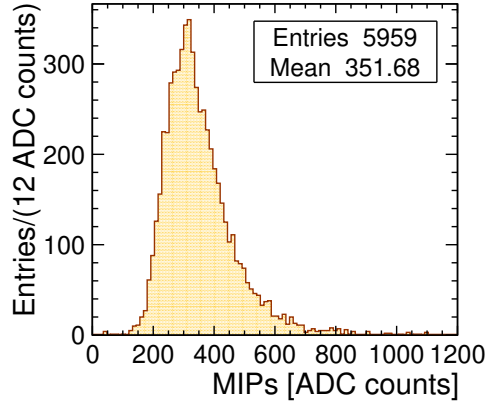


Figure 2: Distribution of the W-AHCAL MIP calibration values for the 5959 calorimeter channels used for the CERN 2010 data.

53 and returns the saturation correction factor which needs to be applied to linearise the ampli-
 54 tude in MIPs.

The amplitude in pixels is obtained by dividing the amplitude of a cell by the corresponding SiPM gain $G_i[\text{ADC}]$:

$$A_i[\text{pixels}] = \frac{A_i[\text{ADC}]}{G_i[\text{ADC}]} \quad (3.2)$$

55 The gain values are obtained from fits of photo-electron spectra taken at low intensity LED
 56 light by a calibration and monitoring LED system.

57 Detailed information about the calibration procedure can be found in [5]. To reduce the noise
 58 contribution, only cells with energy above 0.5 MIPs are used in the analysis of all e^+/e^- and
 59 hadron data.

60 As the SiPM response depends on temperature, only muon runs within a narrow temperature
 61 range ($T = 25 \pm 0.5^\circ \text{C}$) were used for measuring the $A_i^{\text{MIP}}[\text{ADC}]$ calibration constants. The cor-
 62 responding distribution is shown in Fig. 2. From the total of 6480 channels, 92% were calibrated.
 63 The other channels are discarded from the analysis.

64 As calorimeter channels might become inoperable between the MIP calibration measurement
 65 and the physics data taking, the SiPM noise spectrum of the channels is monitored to identify
 66 channels which give no signal anymore, or which give too high signal.

67 These type of channels are identified based on the RMS and the mean value of energy distri-
 68 butions from dedicated random triggers runs:

- 69 • Dead channels: RMS < 20.5 ADC counts.
- 70 • Noisy channels: RMS > 140 ADC counts.

71 For the CERN 2010 data taking period, on average less than 3 % of the total number of calorimeter
 72 channels were identified as noisy or dead, and discarded from the analysis.

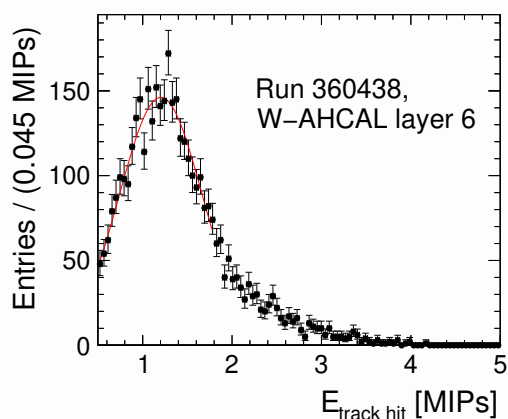


Figure 3: Example fit of the muon peak for layer 6, in run 360438.

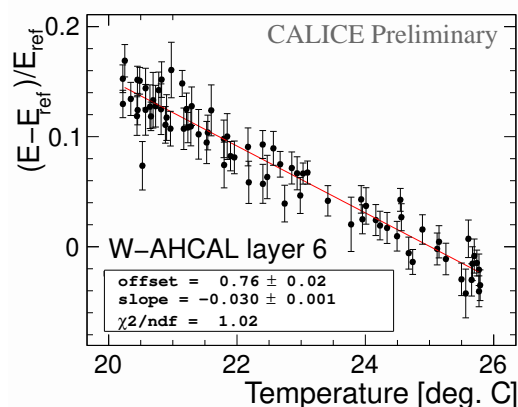


Figure 4: Example of the MIP relative slope measurement for W-AHCAL layer 6.

73 Temperature is measured by five sensors for each calorimeter layer (for details, one can
 74 see [6]). The sensors are horizontally aligned within the layer, and the vertical temperature spread
 75 was found to be of the order of 0.5°C on average [7]. The average calorimeter temperature for the
 76 analyzed runs varies from 20 to 25°C .

77 The dependence of the calorimeter response on temperature was studied per layer. Muon
 78 tracks were identified in pion runs using the track finder described in [8]. In addition, the following
 79 cuts were applied:

- 80 • Number of hits (i.e. active cells) per layer ≤ 2 .
- 81 • Number of active layers ≥ 20 .
- 82 • To reject pions which go through the calorimeter, but might shower in the last layers, events
 83 which have a high energy deposition in any layer (compared to the average energy deposition
 84 per layer) were removed: $E_{\text{layer}} < 5 \cdot E_{\text{layer}}^{\text{median}}$, where E_{layer} is the total energy deposited in one
 85 calorimeter layer, and $E_{\text{layer}}^{\text{median}}$ is the median calculated using the energies deposited in each
 86 layer.

87 For each layer, the distribution of the muon hit energy was fitted to a Gaussian in a range given
 88 by $max \pm 0.5$ MIPs, where max is the position of the maximum in the distribution, as shown in
 89 Fig. 3. From the dependence of the obtained mean muon energy on the temperature in the given
 90 layer, a slope per layer can be obtained. However, as the slopes have to be applied for each channel,
 91 we need to obtain slopes *relative* to a given MIP value, as in the example for layer 6 given in Fig. 4.
 92 The relative slopes were obtained with the following procedure:

- 93 • A reference energy in MIPs, E_{ref} , corresponding to the temperature at which the MIP cali-
 94 brations were measured (25°C), was determined based on the linear fit.
- 95 • The y-axis was converted from energy E to relative difference with respect to the reference
 96 energy E_{ref} : $(E - E_{\text{ref}})/E_{\text{ref}}$.

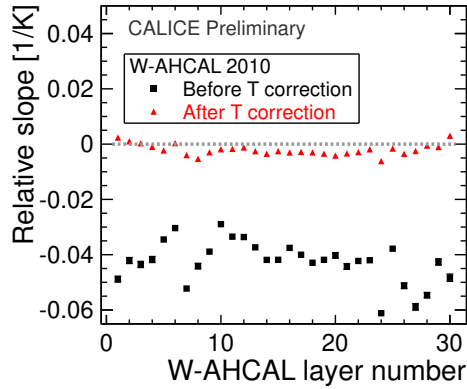


Figure 5: Distribution of the MIP relative slopes per W-AHCAL layer, before and after temperature correction. The average relative slope is $-4.3\%/K$ before the correction, and $-0.2\%/K$ after.

- The linear fit was performed with the new y-axis, and the relative slopes, expressed in percents of MIPs, were obtained.

The distributions of the relative slopes before and after temperature correction are shown in Fig. 5. One can see that after temperature correction the response is equalized at the level of $0.2\%/K$.

4. Simulation

This section describes the test beam geometry as implemented in the GEANT4 [14] based application called Mokka [15], and presents the simulation models that are going to be compared with data.

4.1 Mokka implementation

A schematic representation of the test beam detectors, as simulated with Mokka, is given in Fig. 6.

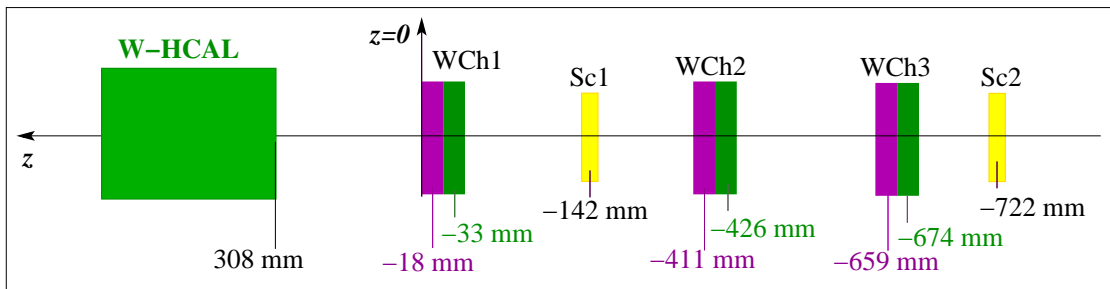


Figure 6: Schematic representation of the CERN 2010 test beam line as implemented in the Mokka model TBCern2010 (not to scale), where *Sc* stands for *scintillator* and *WCh* for *wire chamber*.

It includes three wire chambers, of $110 \times 110 \times 56 \text{ mm}^3$, each with two sections measuring the x and the y position. Based on information from the wire chambers, the track of the incoming

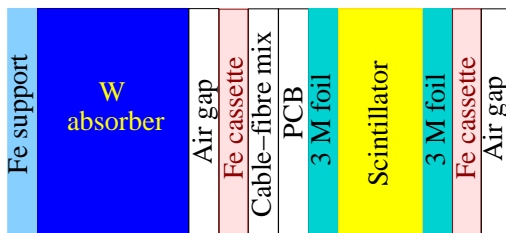


Figure 7: The structure of a W-AHCAL layer as implemented in Mokka (not to scale).

	Thickness [mm]	X_0 [cm]	λ_I [cm]
Fe support	0.5	1.76	16.97
W alloy absorber	10	0.39	10.81
Air gap	2×1.25	30392.10	71013.70
Steel cassette	2×2	1.76	16.97
3M foil	2×0.115	41.12	68.51
PCB	1	17.51	48.39
Cable-fiber mix	1.5	224.37	729.83
Scintillator	5	41.31	68.84
Total	24.73	$2.80 X_0$	$0.13 \lambda_I$

Table 1: Dimensions of the elements of an HCAL layer, as implemented in Mokka. The corresponding radiation length X_0 and nuclear interaction length λ_I are also given.

Material	Mass fraction [%]	Density [g/cm ³]	X_0 [cm]	λ_I [cm]
W	92.99	19.3	0.35	10.31
Ni	5.25	8.91	1.42	15.27
Cu	1.76	8.96	1.44	15.58

Table 2: The components of the tungsten alloy which form the HCAL absorber, with a density of 17.84 g/cm³, as implemented in Mokka. The corresponding radiation length X_0 and nuclear interaction length λ_I are also given.

111 particle is reconstructed. Additionally, two scintillators of $100 \times 100 \times 10$ mm³ are placed on the
 112 beam line. The CALICE coordinate system is a right handed coordinate system, with the origin at
 113 the back plane of the wire chamber closest to the AHCAL, and with the z -axis pointing in the beam
 114 direction.

115 The detailed longitudinal structure of an individual HCAL layer is presented in Fig. 7, with the
 116 exact dimensions given in Table 1. The composition of the tungsten alloy used as absorber is pre-
 117 sented in Table 2, where the radiation and nuclear interaction lengths given are the ones calculated
 118 by GEANT4, version 9.3.p4, when creating the GEANT4 material by hand in the application.

119 4.2 GEANT4 models

120 The physics models in the GEANT4 simulation are combined into so-called **physics lists**, providing
 121 a balance between the level of physics precision and CPU performance. A detailed description can

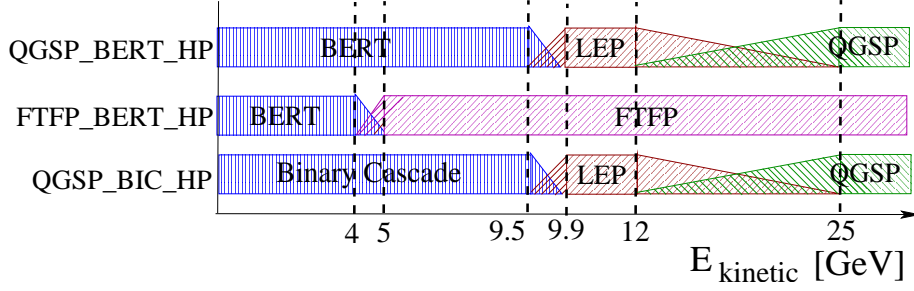


Figure 8: Schematic representation of the GEANT4 physics lists and the validity ranges relevant for this analysis. In the overlap regions between the models, a random choice between the corresponding models is performed, based on the kinetic energy of the incident particle in each interaction.

122 be found for example in [16].

123 Several GEANT4 physics lists were selected in order to compare them with the hadron data.
 124 These include:

- 125 • **LEP:** The **Low Energy Parametrized** model has its origin in the GHEISHA hadronic pack-
 126 age as used with GEANT3. It describes the interactions of long-lived hadrons at all energies,
 127 based on simplified descriptions of interaction mechanisms, with key quantities parametrized
 128 for speed. LEP is used to cover the transition region between physics models in several
 129 physics lists.
- 130 • **BERT:** The **Bertini** cascade model² handles incident nucleons, pions and kaons up to 10 GeV.
 131 The final state of each collision is sampled according to free-particle cross section data. The
 132 target nucleus is treated as an average nuclear medium to which excitons (particle-hole states)
 133 are added after each collision. At the end of the cascade the excited nucleus is represented
 134 as a sum of particle-hole states which is then decayed by pre-equilibrium, nucleus explosion,
 135 fission and evaporation methods. This model reproduces detailed cross section data for these
 136 incident particles in the region below 1 GeV and is expected to do reasonably well in the
 137 multi-GeV region.
- 138 • **QGSP:** The **Quark-Gluon String Precompound** (QGSP) model is built from several com-
 139 ponent models which handle various parts of a high energy collision. The quark-gluon string
 140 (QGS) model is used for interactions of protons, neutrons, pions, kaons and nuclei with en-
 141 ergies from 12 GeV to 100 TeV. It forms QCD strings by pairing a parton from the projectile
 142 hadron with a parton from a target nucleon. The strings are then excited by parton exchange
 143 and decayed to form final state hadrons. The precompound part handles the de-excitation of
 144 the remnant nucleus.
- 145 • **FTFP:** The **FRITIOF** Precompound model, similar to QGSP, is built from several com-
 146 ponent models which handle various parts of a high energy collision. The FRITIOF part

²GEANT4 provides two so-called cascade models, one following the Bertini approach, and one called the Binary cascade, which is more theory-based. Each of these models simulates the initial interaction within the nucleus, producing high-energy secondaries and leaving the nucleus in a highly excited state.

147 handles the formation of strings in the initial collision of a hadron with a nucleon in the nu-
148 cleus. String fragmentation into hadrons is handled by the Lund fragmentation model. The
149 precompound part handles the de-excitation of the remnant nucleus.

150 • **BIC**: The **Binary Cascade** model is valid for incident protons and neutrons with a kinetic
151 energy $E_{\text{kin}} < 10$ GeV, pions with $E_{\text{kin}} < 1.5$ GeV, and light ions with $E_{\text{kin}} < 3$ GeV/A. The
152 target nucleus is modeled by a 3-D collection of nucleons, as opposed to a smooth nuclear
153 medium. The propagation through the nucleus of the incident hadron and the secondaries it
154 produces is modeled by a cascading series of two-particle collisions. These collisions occur
155 according to the particles' total interaction cross section. Secondary particles are created
156 during the decay of resonances formed during the collisions.

157 The physics models are combined into **physics lists**, as shown schematically in Fig. 8. With
158 the energy studied in this paper ($1 \text{ GeV} < p_{\text{beam}} \leq 10 \text{ GeV}$), the Bertini and FRITIOF models are
159 probed for pions, while for protons the Binary Cascade model is tested in addition. As the QGSP
160 model is only valid from $E_{\text{kin}} > 12$ GeV, it is not tested in the analyzed energy range.

161 QGSP_BERT is the default list for the CMS and ATLAS detector simulations, as it has proven
162 to show the best agreement with test beam data for energy response, e/π ratio, energy resolution
163 and pion shower profiles. FTFP_BERT is an alternative to QGSP_BERT, which is expected to
164 show better proton shower profiles, but energy responses which exceed measurements.

165 As the W-AHCAL uses tungsten as absorber material, neutrons are expected to play an impor-
166 tant role in hadron interactions in this calorimeter (for a detailed discussion on the role of neutrons
167 in calorimetry see for example [17]). Therefore the above mentioned physics lists are combined
168 with the data driven Neutron **High Precision** (HP) Models and Cross Sections, which treat the de-
169 tailed simulation of the interaction, transportation, elastic scattering and capture of neutrons with
170 energies below 20 MeV.

171 A comparison of the QGSP_BERT list with and without the High Precision package is shown
172 in Fig. 9, for the calorimeter response to 10 GeV π^- . The data were reconstructed as described in
173 Sect. 3, while the simulated data were digitized as described in Sect. 4.3. It can be seen that adding
174 HP improves the agreement with data, although the impact is not as significant as for example for
175 the timing measurements presented in [18].

176 It should be noted that the non-HP physics lists use LEP for the neutron capture simulation.

177 The FTFP_BERT_HP physics list was not included in the GEANT4 release (version 9.3.p4),
178 but we received it from the GEANT4 developers in order to make a comparison with a FRITIOF
179 based model.

180 Since the electromagnetic model is the same for all GEANT4 physics lists, the electromagnetic
181 data will be compared with the QGSP_BERT physics list only.

182 4.3 Generation and Digitization of the Simulation

183 The events are generated with Mokka, using one of the selected physics lists described in Sec-
184 tion 4.2.

185 Especially for the electromagnetic showers, where a limited number of tiles are involved (com-
186 pared to the hadron shower case), it is important that in the simulation we have the same configu-

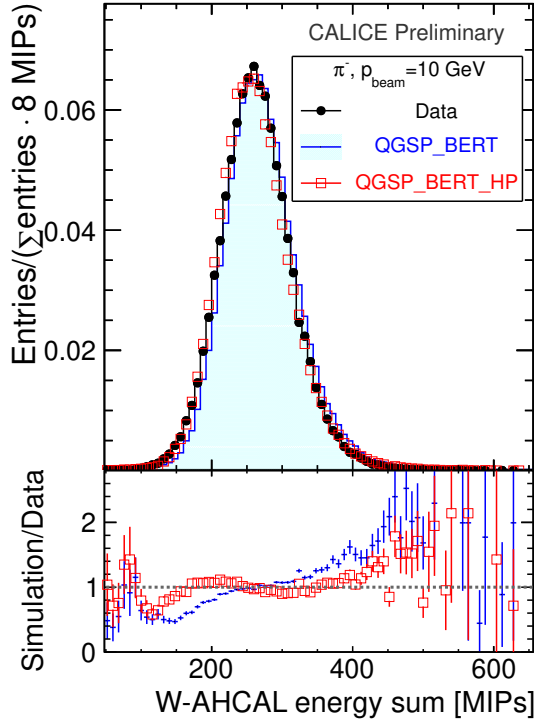


Figure 9: Energy distribution for 10 GeV π^- : comparison of data with QGSP_BERT and QGSP_BERT_HP. In the lower part, the ratio of the two simulation physics lists to data is shown.

187 ration of active tiles as in data. The position of the particle gun and the beam spread are taken from
 188 data, based on wire chamber information.

189 To compare simulation with data, one needs to consider realistic detector effects which occur in
 190 addition to the plain particle interaction and energy deposition. This is done both at the generation
 191 and digitization level.

192 Already at the generation step, the following aspects are taken into account:

- 193 ● **Signal shaping time of the readout electronics:** To emulate it, only hits within a time
 194 window of 150 nsec (corrected for the time of flight) are accepted.
- **Non-linearity of the light output:** In the case of plastic scintillator, the light output per unit
 length has a non-linear dependence on the energy loss per unit length of the particle's track.
 This behavior is described by the so-called *Birks' law* [20]:

$$\frac{dL}{dx} \propto \frac{1}{1 + k_B \cdot dE/dx}, \quad (4.1)$$

195 where dL/dx represents the light output per unit length, dE/dx is the energy lost by the
 196 particle per unit length of its path, and k_B is a material dependent factor (Birks constant).
 197 The Birks law is applied to the W-AHCAL hits, using a factor of $k_B = 0.07943 \text{ mm/MeV}$.

198 Next, the events are subject to a process called digitization. The same sets of calibration values
 199 and of dead channels is used in the digitization, as for the reconstruction of the experimental data.

200 In a first digitization step, the simulated energy (in GeV) is converted in MIPs based on a MIP to
 201 GeV factor obtained from fitting with a Landau function the single hit energy spectra of simulated
 202 muons. Then the detector granularity, the light sharing between the tiles, the non-linear SiPM
 203 response due to saturation, the statistical smearing of the detector response at the pixel scale, and
 204 the contribution from electronic noise (obtained from data) are taken into account.

205 At this stage, the energy of the simulated hits is expressed in ADC counts, and is given as
 206 input to the same calibration procedure as for the data (see Eq. 3.1).

207 The digitization of the CALICE AHCAL hits is described in detail in [9]. We use a cross-talk
 208 factor of 10%, with a MIP to GeV factor of 805 keV. More details can be found in Appendix B.

209 5. Analysis of the e^-/e^+ data

210 When analyzing data from a hadronic calorimeter, one is most interested in hadron data. However,
 211 as the underlying physics of electromagnetic showers is best understood, the analysis of e^+/e^-
 212 data is used to validate the implementation of the detector material and response in the simulation,
 213 as well as the calibration chain. Mistakes in the simulated material would result in discrepancies
 214 between data and theoretical models, while imperfections in the treatment of the saturation effects,
 215 for example, would result in a deviation of the reconstructed electromagnetic energy from the linear
 216 dependence on the beam momentum.

217 The electromagnetic analysis is also important for the study of the degree of (non)compensation
 218 of the hadron calorimeter, which is expressed in the e/h ratio, i.e. the ratio between the calorimeter
 219 response to leptons and to hadrons.

220 This section describes the selection of e^+/e^- data, as well as their analysis and the comparison
 221 with the simulation.

222 The analyzed runs³ are given in Appendix A. The beam is composed of electrons, muons,
 223 pions, and also protons (in case of positive beam polarity).

224 5.1 Data selection

225 The first level of selection is based on Cherenkov triggers. However, as these triggers are not 100%
 226 efficient, it was necessary to apply additional cuts.

227 To increase the purity of the electromagnetic data we have used the clustering algorithm de-
 228 scribed in [21]. While hadrons are expected to go deep into the calorimeter, electrons start to
 229 shower already in the first calorimeter layer, and most of the shower is contained within the first
 230 five layers.

After applying the Cherenkov selection, there is still a small fraction (of the order of a few
 percents) of hadron and muon events in the data sample. To reject them, we apply a cut on the
 center of gravity in z , z_{cog} , defined as:

$$z_{\text{cog}} = \frac{\sum_i E_i \cdot z_i}{\sum_i E_i}, \quad (5.1)$$

³There are more positive than negative polarity runs. The reason is that we started the data taking with negative
 polarity, and we needed some time to study the correct Cherenkov settings. Therefore negative runs from the beginning
 of the data taking had Cherenkov pressure for which the counters were not efficient, so they are not included in the
 analysis.

231 where z_i is the z -position of the cluster hits, and E_i is their energy. We only accept events with one
 232 cluster which has the center of gravity along the beam axis in the first part of the calorimeter. i.e.
 233 with $z_{\text{cog}}^{\text{cluster}} < 400$ mm, which corresponds to approximately 3 calorimeter layers, and is safe for
 234 the analyzed energy range ($E \leq 6$ GeV).

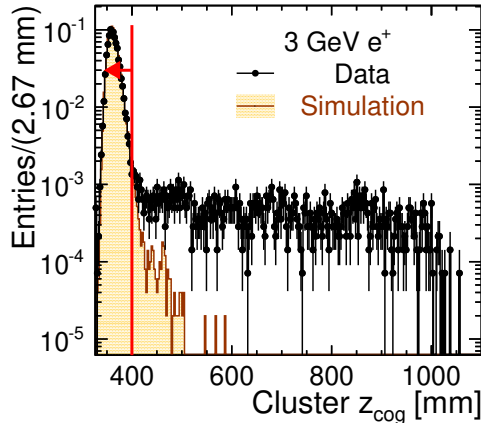


Figure 10: Distribution of the z_{cog} of clusters identified in 3 GeV e^+ events.

235 The z_{cog} distribution of clusters identified in events tagged by the Cherenkov triggers as be-
 236 ing e^+ , for the 3 GeV case, is shown in Fig. 10. The peak is due to e^+ events⁴, while the long
 237 tail is due to muon-like events and to hadrons which shower late in the calorimeter. Requesting
 238 $z_{\text{cog}}^{\text{cluster}} < 400$ mm will reject these events.

239 To reduce the influence of noise in the e^-/e^+ events, the calorimeter hits are selected for
 240 subsequent analysis if they fulfill the following criteria:

- 241 • Are within the first 20 calorimeter layers.
- 242 • Are within the central 3×3 cm² tiles.

243 5.2 The Novosibirsk fit function

244 If all the energy is deposited in the calorimeter⁵, one naively expects a Gaussian shape of the
 245 distribution of the total visible energy in the calorimeter. However, the e^-/e^+ energy spectra have
 246 a non-Gaussian shape, with tails at high energies, as can be seen in the example for 1 GeV positrons
 247 shown in Fig. 11. For completeness, the energy sum distributions for the analyzed beam momenta
 248 are presented in Fig. 13. We considered only runs up to 6 GeV; for higher energies, the electron
 249 content in the beam was too low (of the order of a few hundreds of events, or lower).

250 After carefully checking for noisy cells, we arrived to the conclusion that the high energy tails
 251 are an artifact of the limited number⁶ of active cells in an electromagnetic shower. On average,

⁴The active plane in the first calorimeter layer is positioned at $z = 328$ mm.

⁵Energy leaking out of the calorimeter would induce low energy tails in the energy distribution, while noisy channels would measure unphysical high energies, therefore inducing tails on the right side of the distribution.

⁶The central limit theorem states that the distribution of an average tends to be Gaussian for a large number of samples, even when the distribution from which the average is computed is decidedly non-Gaussian.

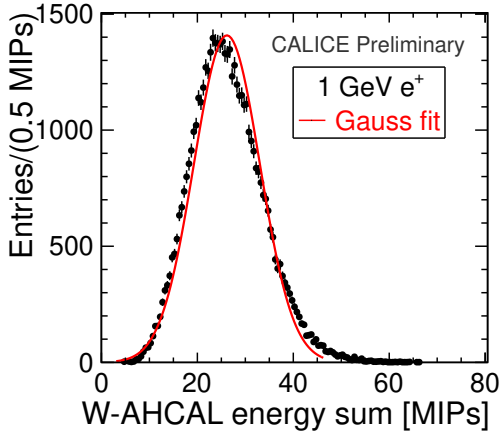


Figure 11: Energy sum distribution for 1 GeV positrons fitted with a Gaussian function.

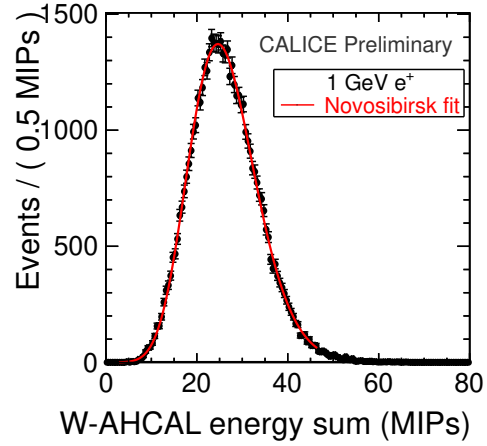


Figure 12: Energy sum distribution for 1 GeV positrons fitted with the Novosibirsk function.

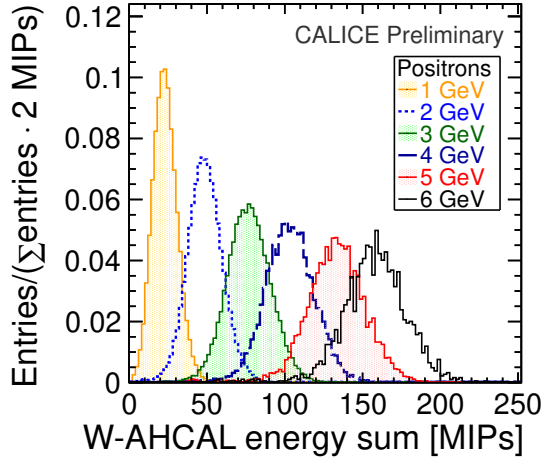


Figure 13: The visible energy deposited in the W-AHCAL by positrons with energies from 1 to 6 GeV.

252 about 17 cells are active in an electromagnetic shower induced by a 1 GeV particle, and about
 253 38 cells in the 6 GeV case. The energy spectra of individual cells, after pedestal subtraction, are
 254 exponential. With increasing number of active cells, the total energy distribution becomes more
 255 and more Gaussian. The high energy tails are also present in the simulation, at generator level, i.e.
 256 before including any detector effects.

The electron energy spectra are fitted with the Novosibirsk fit function, which accounts for the high energy tails, using RooFit [22]. This function is defined as [23]:

$$f(x) = A \cdot \exp \left(-0.5 \cdot \left(\frac{\ln^2 [1 + \Lambda \cdot \tau \cdot (x - \mu)]}{\tau^2} + \tau^2 \right) \right) \quad (5.2)$$

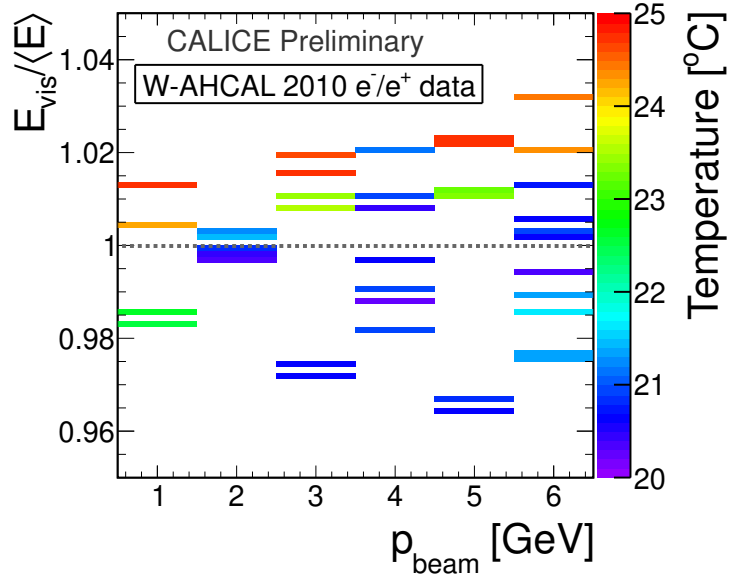


Figure 14: Ratio between the e^-/e^+ reconstructed energy and the average energy of all selected runs at a given beam momentum.

where

$$\Lambda \equiv \frac{\sinh(\tau \cdot \sqrt{\ln 4})}{\sigma \cdot \tau \cdot \sqrt{\ln 4}}, \quad (5.3)$$

with μ the peak position, σ the width, and τ the tail parameter. For values of τ close to zero, σ relates to the width of a Gaussian distribution.

An example fit for 1 GeV positrons, together with the fit results, is given in Fig. 12. The fit range is $\pm 3\sigma$ around the peak of an initial fit with the same function. The energy sum distributions and the corresponding fits for the analyzed e^-/e^+ data sample can be found in Appendix C.

5.3 Systematic uncertainties

The measurement of the calorimeter response is subject to systematic uncertainties. These uncertainties come from two main sources: the calibration procedure⁷ (including the methods used to determine the calibration constants and to correct for temperature variations), and the event selection, which for the moment is not considered.

To estimate the systematic error due to the first source, we did the following:

- We selected runs with at least 300 e^-/e^+ events, as presented in Section 5.1, and performed the fit described in Section 5.2 to determine the mean value of the visible energy E_{vis} .
- For a given beam momentum, we calculated an average reconstructed energy $\langle E \rangle$ from all runs at that beam momentum.
- Then, for each run, we calculated the ratio of the corresponding E_{vis} to the average of all runs at one beam momentum.

⁷For a detailed discussion on systematic uncertainties due to the calibration procedure, see for example [21].

274 The distribution of the e^-/e^+ visible energy is shown in Fig. 14. The majority of e^- runs are at
 275 low temperatures, while most of the e^+ runs are closer to 25° C, which is the temperature at which
 276 the MIP calibration constants were measured. As the precision of the temperature correction is
 277 limited, we expect larger systematic effects for the e^- case. However, the large spread observed for
 278 the 4 GeV runs, which are at similar temperatures, suggests that there might be other effects which
 279 are not yet identified.

280 The largest variation of the ratio, with an RMS of 2.5%, is observed for the 5 GeV case.
 281 Overall, the average RMS is **1.5%**. This value is considered to be our systematic uncertainty.

282 5.4 Electromagnetic response and energy resolution

283 The calorimeter response for electromagnetic showers is expected to be linear with the beam mo-
 284 menta. This dependence is shown in Fig. 15. The mean visible energy $\langle E_{\text{vis}} \rangle$ is given by the mean
 285 (the μ parameter) of the Novosibirsk fitting function described in Section 5.2. The lines indicate
 286 a fit with the function $E_{\text{vis}} = u + v \cdot p_{\text{beam}}$, where u is the offset, and v the slope. The fit results are
 287 given in Table 3. The obtained negative offset is the combined effect of the 0.5 MIP threshold (loss
 288 of energy) and the detector noise (addition of energy).

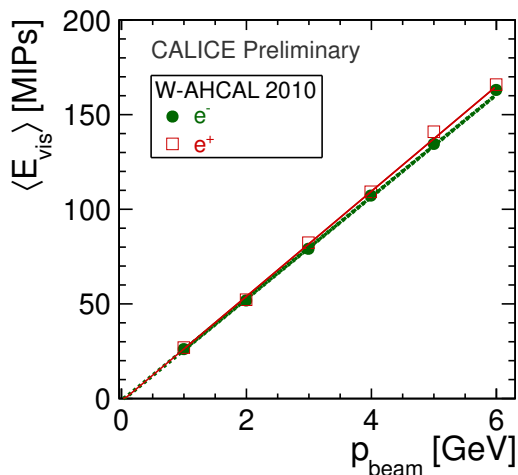


Figure 15: Dependence of the mean visible energy on the beam momenta for 2010 e^+/e^- W-AHCAL data. The error bars are given by the quadratic sum of the statistical and systematic errors. The lines indicate fits with the function $E_{\text{vis}} = u + v \cdot p_{\text{beam}}$.

Parameter	e^-	e^+
u [MIPs]	-1.28 ± 0.57	-1.56 ± 0.58
v [MIPs/GeV]	26.98 ± 0.29	27.77 ± 0.30
χ^2/ndf	3.2/4	11.0/4

Table 3: Fit parameters of the dependence of the mean visible energy on the beam momenta for the 2010 e^-/e^+ W-AHCAL data. The error are given by the quadratic sum of the statistical and systematic errors.

289 The agreement of the electromagnetic energy scale in MIPs/GeV between e^- and e^+ is not
 290 very good; the difference corresponds to about two standard deviations. This may be due to the
 291 fact that the e^- and e^+ data systematically populate opposite ends of the considered temperature
 292 range such that residual imperfections of the corrections may be larger than our evaluated average
 293 spread of 1.5% given as systematic error for runs taken at the same energy.

294 The residuals to the fit are shown in Fig. 16, where $\langle E_{\text{rec}} \rangle$ [GeV] = $(\langle E_{\text{vis}} \rangle$ [MIPs] - u)/ v , with
 295 the v parameters given in Table 3. The linearity is within $\pm 4\%$ ($\pm 2\%$) for e^+ (e^-).

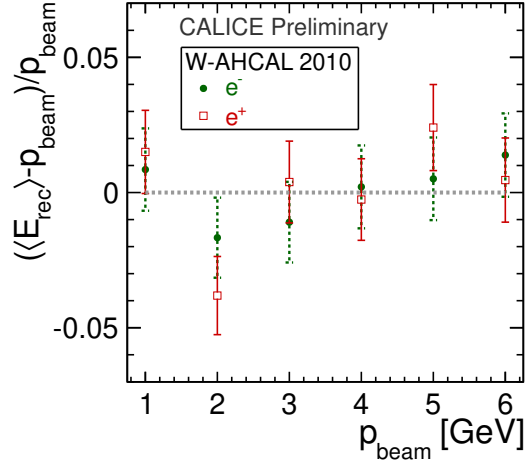


Figure 16: Deviations from linearity for the W-AHCAL 2010 e^-/e^+ data, with respect to their own individual fits. The error bars are given by the statistical and systematic errors added in quadrature.

The electromagnetic energy resolution is presented in Fig. 17. The fit function is:

$$\frac{\sigma_E}{E} = \frac{a}{\sqrt{E [\text{GeV}]}} \oplus b \oplus \frac{c}{E [\text{GeV}]}, \quad (5.4)$$

where:

- a is the **stochastic term**, which takes into account the statistical fluctuations in the shower detection. It also contains contributions from cells with physical energy deposits, for which the signal is smeared by noise.
- b is the **constant term**, which is dominated by the stability of the calibration, but includes also detector instabilities (i.e. non-uniformity of signal generation/collection, loss of energy in dead materials);
- c is the **noise term**, the equivalent of the electronic noise in the detector, which includes noise from cells without physical energy deposits. This term depends on the analysis, more specifically on the considered fiducial volume.

The noise term is fixed to the spread (RMS) of the energy sum distribution of randomly triggered noise events inside the beam spill, considering only the central $3 \times 3 \text{ cm}^2$, contained in the first 20 layers, as done for the selection of the electromagnetic data (Sect. 5.1). The corresponding values in MIPs are given in Table 5. These values are converted to GeV using the ν parameters of the fit given in Table 3: $E[\text{GeV}] = E[\text{MIPs}]/\nu$.

The measured e^+ energy resolution for W-AHCAL and other CALICE hadron calorimeters are given in Table 6. The comparison should be done with a grain of salt, as the energy ranges and the fit procedure differ. In the Fe-AHCAL case, the energy spectra are fitted with a Gaussian in a region defined by the central 90% of the statistics [24], or in $\pm 2\sigma$ range [5], while for the DHCAL Gaussian fits in the full range are applied.

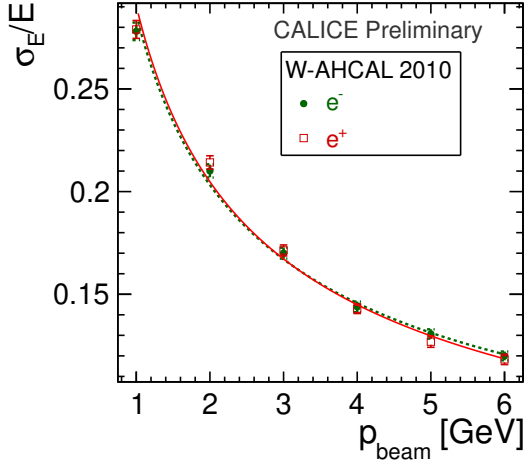


Figure 17: Energy resolution for the 2010 e^+/e^- W-AHCAL data. The error bars are given by the quadratic sum of the statistical and systematic errors.

Parameter	e^-	e^+
a [%]	28.1 ± 0.4	28.7 ± 0.4
b [%]	3.7 ± 0.9	1.6 ± 2.3
c [MeV]	37	38
χ^2/ndf	10.3/4	19.6/4

Table 4: Parameters of the energy resolution fits for the 2010 e^+/e^- W-AHCAL data.

Runs	Noise RMS [MIPs]
Positive polarity	1.06 ± 0.02
Negative polarity	1.01 ± 0.03

Table 5: RMS of the energy distribution for randomly triggered events inside the beam spill, for the central $3 \times 3 \text{ cm}^2$ cells, contained in the first 20 calorimeter layers.

Detector	Particle type	p_{beam}	a [%]	b [%]	c [MeV]	χ^2/ndf
Fe-AHCAL	e^+/e^-	1, 2, 4, 6, 10 GeV and 20 GeV	21.7 ± 0.2	0 ± 0.8	50	?
	e^+	10-50 GeV	21.9 ± 1.4	1.0 ± 1.0	58	?
DHCAL	e^+	2, 4, 8, 12, 20 and 32 GeV	26.8 ± 0.4	0	129.5 ± 1.2	7.6/4
W-AHCAL	e^+	1-6 GeV	28.7 ± 0.4	1.6 ± 2.3	38	19.6/4

Table 6: Parameters of the e^+ energy resolutions for the CALICE hadron calorimeters Fe-AHCAL [24], [5], DHCAL [25] and W-AHCAL. The noise term is fixed in the W-AHCAL case to the RMS of the energy distribution in randomly triggered events, considering only cells in the same fiducial volume as for the electromagnetic data.

316 As expected, the e^+ energy resolution for the W-AHCAL case is not as good as in the Fe-AHCAL
317 case, although the absorber material in the detector corresponds to the same number of interaction
318 lengths, and the readout device is the same. This is due to the difference in the X_0 values between
319 the two absorbers (see Table 1). In the Fe-AHCAL case, we have $16 + 2 \cdot 2 \text{ mm}$ Fe absorber per
320 layer, while in the W-AHCAL case, there are $10 \text{ mm W} + 4.5 \text{ mm Fe}$ per layer. In consequence, in
321 the latter case we sample about 3 times less within an electromagnetic shower.

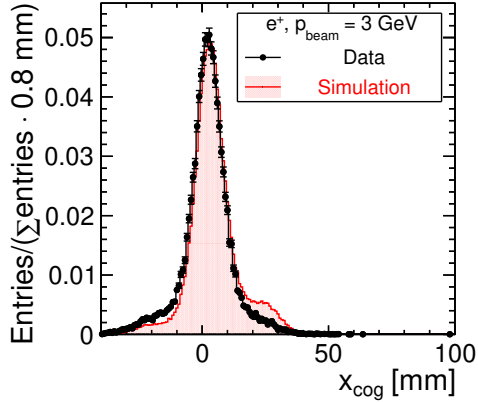


Figure 18: Distribution of x_{cog} for a 3 GeV positron in data and in the simulation.

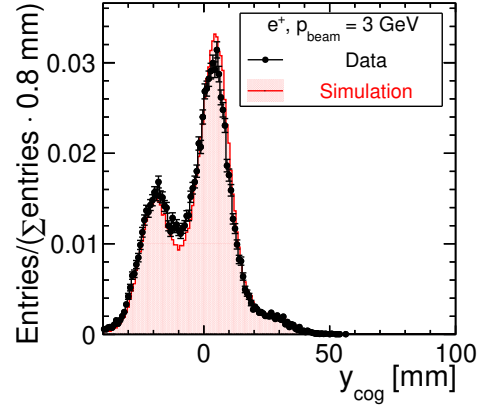


Figure 19: Distribution of y_{cog} for a 3 GeV positron in data and in the simulation.

322 The electromagnetic energy resolutions obtained using Novosibirsk fits are compared to the
 323 results obtained with Gaussian fits in a region containing 80% of the statistics in Appendix D.
 324 Applying Gaussian fits in this limited range gives results similar to the case with Novosibirsk fits
 325 in a $\pm 3\sigma$ region.

326 5.5 Comparison with simulation

The events are generated and digitized as explained in Sect. 4.3. An example of the level of match-
 ing between data and simulation for the beam profile is given in Figs. 18 and 19, where x_{cog} and
 y_{cog} are the coordinates of the W-AHCAL center of gravity, defined as:

$$x_{\text{cog}} = \frac{\sum_i x_i \cdot E_i}{\sum_i E_i} \text{ and } y_{\text{cog}} = \frac{\sum_i y_i \cdot E_i}{\sum_i E_i} \quad (5.5)$$

327 where x_i/y_i are the hit coordinates, and E_i is the energy of the hit.

328 The level of agreement is satisfactory.

329 For the energy sum distribution, an example is given in Fig. 20. Comparisons of data with the
 330 simulation are also done for the dependence of the mean e^+ visible energy on the beam momenta
 331 in Fig. 21. The level of agreement between data and the simulation for the e^+ visible energy is
 332 good, the deviation does not exceed 2% for the analysed energy range.

333 The positron energy resolution fits for data and simulation are shown in Fig. 22, and the fit
 334 results are presented in Table 8. The longitudinal shower profiles, i.e. average visible energy per
 335 layer, for 1 and 5 GeV positron candidates are shown in Figs. 23 and 24.

336 The data are well reproduced, both for integrated variables like the visible energy, and for the
 337 longitudinal profiles.

338 Having validated the simulation, we can proceed with the hadron shower analysis.

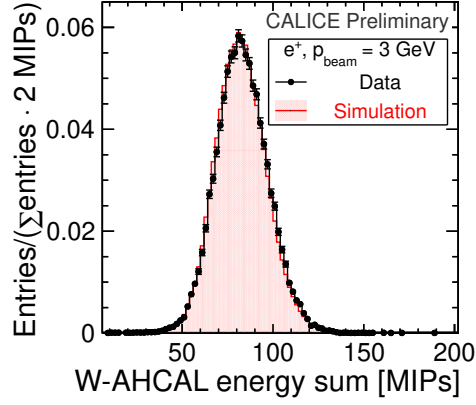
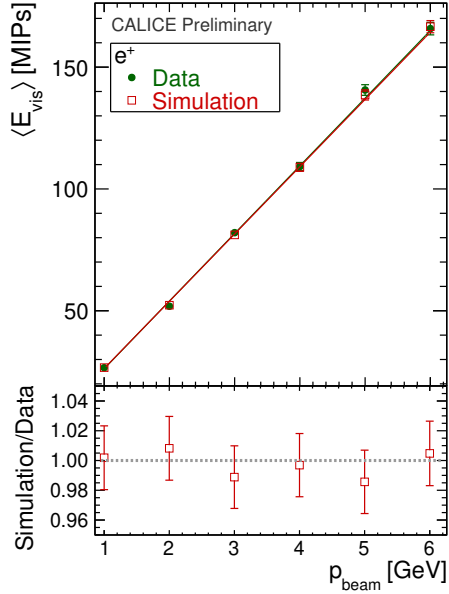


Figure 20: Energy sum distribution for 3 GeV positrons: comparison of data with simulation.



Parameter	Data	Simulation
u [MIPs]	-1.56 ± 0.58	-1.30 ± 0.58
v [MIPs/GeV]	27.77 ± 0.30	27.61 ± 0.29
χ^2/ndf	11.0/4	6.9/4

Table 7: Fit parameters of the dependence of the mean positron visible energy on the beam momenta: comparison of data with simulation.

Figure 21: Dependence of the mean visible positron energy on the beam momenta: comparison of data with simulation. The error bars are given by the quadratic sum of the statistical and systematic errors. The lines indicate fits with the function $\langle E_{vis} \rangle = u + v \cdot p_{beam}$. In the lower part, the ratio between the simulation and data is shown.

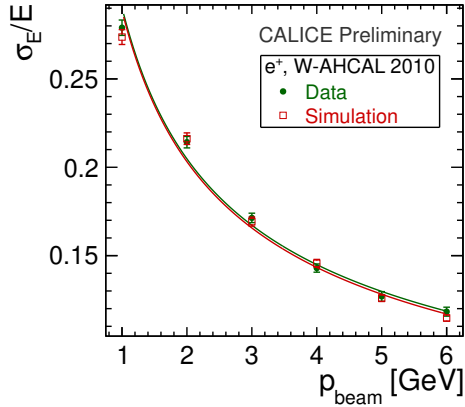


Figure 22: Energy resolution for e^+ events: comparison of data with simulation. The error bars are given by the quadratic sum of the statistical and systematic errors.

Parameter	Data	Simulation
a [%]	28.7 ± 0.4	28.6 ± 0.2
b [%]	1.6 ± 2.3	0 ± 2.6
c [MeV]	38	38
χ^2/ndf	19.6/4	34.7/4

Table 8: Parameters of the positron energy resolution fits for data and the simulation.

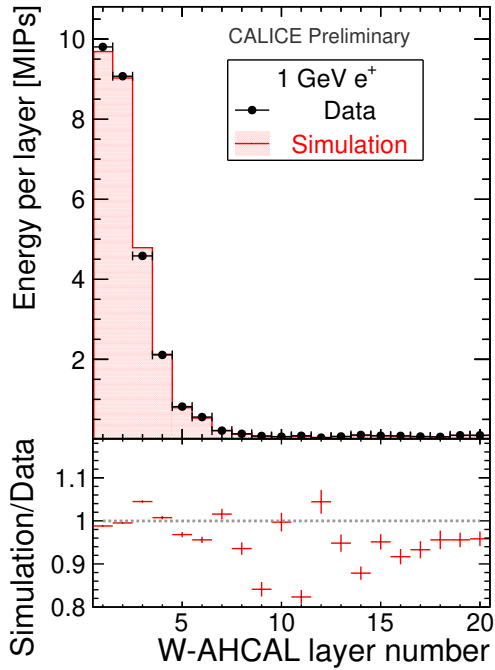


Figure 23: Longitudinal shower profile for 1 GeV e^+ candidates: comparison of data with simulation.

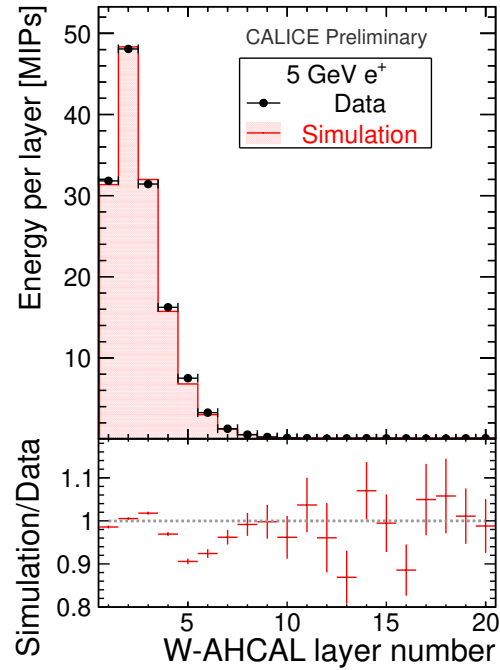


Figure 24: Longitudinal shower profile for 5 GeV e^+ candidates: comparison of data with simulation.

339 6. Analysis of the π^-/π^+ data

340 This section describes the cuts used to select π^+/π^- events, as well as the obtained results.

341 To reject muons without the help of a tail catcher, we use the tracking algorithm from [26],
 342 combined with the clustering algorithm described in [21]. A set of cuts was developed by carefully
 343 checking the event displays, and the impact on the analyzed data sample.

344 The events which fulfill the following cuts are considered to be either muon-like events, or late
 345 showering hadrons, and are rejected if any of the following conditions apply:

- 346 1. A track is identified which ends in layer ≥ 15 , has a small angle ($\cos \phi \geq 0.99$), and traverses
 347 at least 14 layers.
- 348 2. At least two tracks are identified, which have a small angle ($\cos \phi > 0.94$), each track traversing
 349 at least six layers.
- 350 3. At least one track is identified with hits in layer 29 or 30, and which traverses at least ten
 351 layers.
4. If there are two or more high energy hits (high compared to the energy of most of the hits)
 on the track of the muon, or of the punch-through hadron, then two aligned clusters might be
 identified. If the first cluster is positioned in the first calorimeter half, and the second in the
 last calorimeter part

$$z_{\text{cog}}^{\text{cluster 1}} < 727.5 \text{ mm, and } z_{\text{cog}}^{\text{cluster 2}} \geq 727.5 \text{ mm} \quad (6.1)$$

it is checked if they are aligned in x and y :

$$|x_{\text{cog}}^{\text{cluster 1}} - x_{\text{cog}}^{\text{cluster 2}}| < \text{tile size} = 30 \text{ mm and} \quad (6.2)$$

$$|y_{\text{cog}}^{\text{cluster 1}} - y_{\text{cog}}^{\text{cluster 2}}| < \text{tile size} = 30 \text{ mm.} \quad (6.3)$$

If the two clusters by are separated by a smaller distance, but by at least 6 layers, i.e. about
 150 mm:

$$|z_{\text{cog}}^{\text{cluster 1}} - z_{\text{cog}}^{\text{cluster 2}}| > 150 \text{ mm,} \quad (6.4)$$

they are considered as belonging to a muon track if:

$$|x_{\text{cog}}^{\text{cluster 1}} - x_{\text{cog}}^{\text{cluster 2}}| < \text{tile size}/2 = 15 \text{ mm and} \quad (6.5)$$

$$|y_{\text{cog}}^{\text{cluster 1}} - y_{\text{cog}}^{\text{cluster 2}}| < \text{tile size}/2 = 15 \text{ mm.} \quad (6.6)$$

- 352 5. If no cluster is identified, then the event most probably contains only noise hits, or the hadron
 353 showered before the calorimeter, while only the low energy tail of the shower reaches the
 354 detector.
- 355 6. If the hadron shower start is late, a cluster might be found in the second half of the calorime-
 356 ter: $z_{\text{cog}}^{\text{cluster}} > 727.5 \text{ mm}$. This may also happen if the muon track contains a hit at the end of
 357 the calorimeter, which has higher energy than the other hits.

- 358 7. At least one track is identified with hits in layer 29 or 30, which has an angle of zero degrees,
359 i.e. $\cos \phi = 1$, where ϕ is the angle between the track and the z -axis.
- 360 8. The identified track passes through more than 20 layers.
- 361 9. At least two tracks are identified, and at least two of them have $\cos \phi \geq 0.9$.
- 362 10. Two or more tracks are identified, from which at least two traverse more than ten layers.
- 363 11. Due to dead channels, or in case the particle enters at an angle, several track segments might
364 be identified instead of one track only. If there are three tracks, each with a small angle
365 ($\cos \phi > 0.9$) and each traversing at least six layers, the event most probably contains a muon
366 or a punch-through hadron.
12. No track is identified, but a cluster with $z_{\text{cog}}^{\text{cluster}} > 600$ mm and close to the beam axis:

$$|x_{\text{cog}}^{\text{cluster}}| < \text{tile size} = 30 \text{ mm and } |y_{\text{cog}}^{\text{cluster}}| < \text{tile size} = 30 \text{ mm.} \quad (6.7)$$

- 367 13. In addition, events with low number of hits are rejected (see Table 9).

368 The fraction of events rejected by the above described cuts is given for π^+ events in Table 10.
369 These cuts are also applied in the simulation, in order to remove muons from pions decaying in
370 flight.

p_{beam} [GeV]	$N_{\text{hits}}^{\text{min}}$
3	15
4	15
5	25
6	30
7	30
8	35
9	35
10	35

Table 9: The cuts applied on the minimum number of hits $N_{\text{hits}}^{\text{min}}$ in hadron events.

Cuts	π^+ , fraction of rejected events	
	$p_{\text{beam}} = 3 \text{ GeV}$	$p_{\text{beam}} = 10 \text{ GeV}$
1	32%	26%
2	6%	10%
3	3%	6%
4	2%	4%
Others	2%	4%
All	45%	50%

Table 10: Fraction of rejected events after cuts selecting muon and late showering hadrons in π^+ events, with respect to the Cherenkov trigger selection.

371 The energy distributions for π^+ with a beam momentum of 3 and 10 GeV, before and after
372 the different hadron selection cuts, are shown in Figs. 25 and 26. While for high energy hadrons
373 the muon peak is well separated from the hadron peak, for low energies the two peaks overlap,
374 and it becomes increasingly difficult to select the right particle. The analysis of hadrons with beam
375 momenta of 1 and 2 GeV are not included in this paper due to difficulties in a reliable selection of
376 hadrons at these low energies.

377 The muon rejection can be also visualized in the distributions of the number of hits vs. z_{cog}
378 shown in Appendix E.

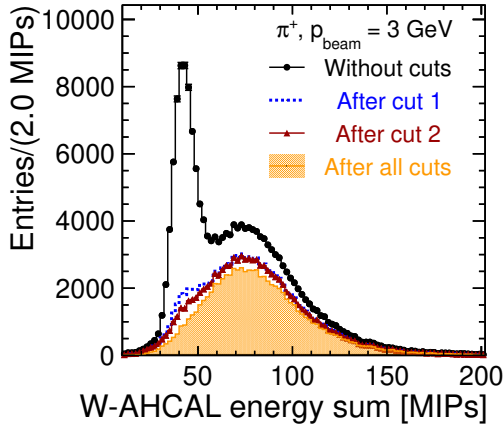


Figure 25: The visible energy deposited in the W-AHCAL by π^+ with a beam momentum of 3 GeV, before and after the different hadron selection cuts.

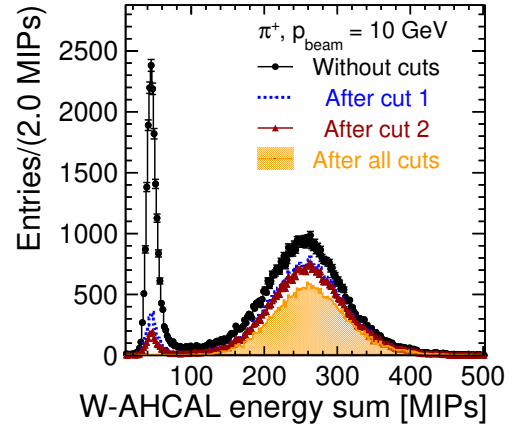


Figure 26: The visible energy deposited in the W-AHCAL by π^+ with a beam momentum of 10 GeV, before and after the different hadron selection cuts.

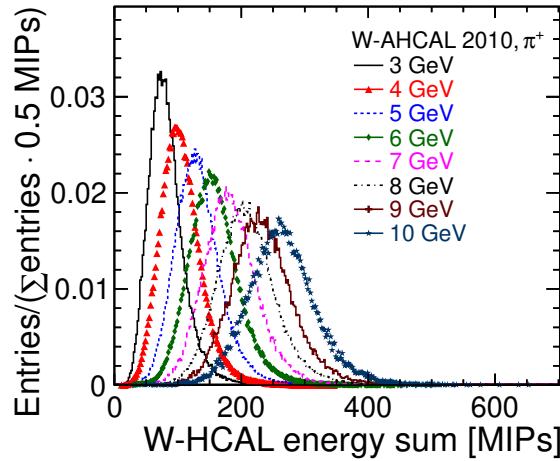


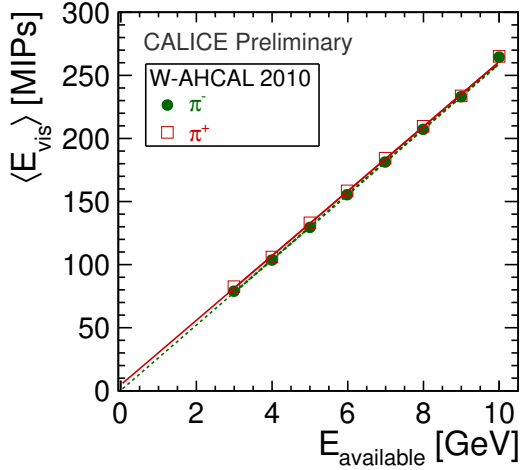
Figure 27: The visible energy deposited in the W-AHCAL by π^+ with energies from 3 to 10 GeV.

The energy distributions for π^+ in the energy range from 3 to 10 GeV are presented in Fig. 27. It is obvious that for low energies the distributions are non-Gaussian. In order to measure the hadron energy resolution, and to take this non-Gaussian shape into account, we use:

$$\frac{\sigma_E}{E} = \frac{RMS}{Mean}, \quad (6.8)$$

379 with *RMS* and *Mean* obtained directly from the histogram statistics.

The dependence of the mean visible energy vs. the available energy $E_{\text{available}}$ is shown in Fig. 28, where $E_{\text{available}}$ is the energy available for deposition in the calorimeter in case of a pion,



Parameter	π^-	π^+
u [MIPs]	0.27 ± 1.86	4.64 ± 1.92
v [MIPs/GeV]	25.90 ± 0.36	25.61 ± 0.37
χ^2/ndf	2.2/6	2.7/6

Table 11: Fit parameters of the dependence of the mean π^-/π^+ visible energy.

Figure 28: Dependence of the mean visible energy on the beam momenta for the 2010 W-AHCAL π^-/π^+ data. The error bars are given by the quadratic sum of the statistical and systematic errors. The lines indicate fits with the function $\langle E_{\text{vis}} \rangle = u + v \cdot E_{\text{available}}$.

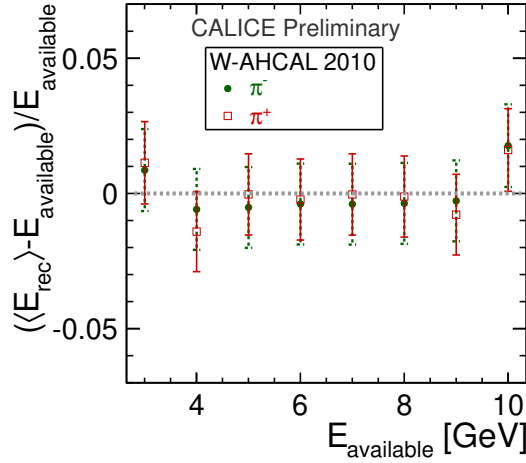
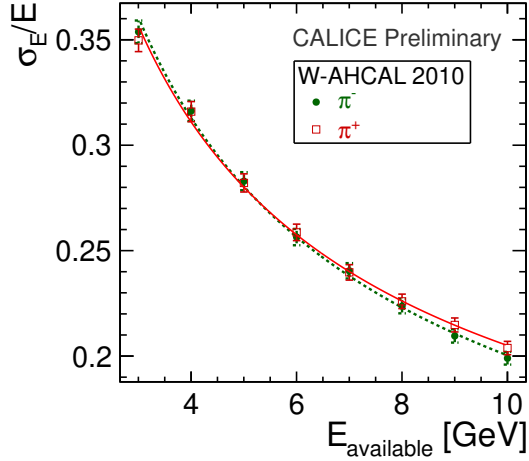


Figure 29: Deviations from linearity for the W-AHCAL 2010 π^-/π^+ data.

and which is given by:

$$E_{\text{available}} = \sqrt{p_{\text{beam}}^2 + m_{\pi}^2}, \quad (6.9)$$

380 where m_{π} is the pion mass. The lines indicate a fit with the function $\langle E_{\text{vis}} \rangle = u + v \cdot E_{\text{available}}$. The
 381 slope is similar for π^+ and π^- , but the offsets differ slightly. This might be due to a difference
 382 in the average noise level between the negative and positive polarity runs. The deviation from
 383 linearity is presented in Fig. 29, where $\langle E_{\text{rec}} \rangle$ [GeV] = $(\langle E_{\text{vis}} \rangle$ [MIPs] - u)/ v , with the v parameters



Parameter	π^-	π^+
a [%]	61.9 ± 1.0	60.3 ± 1.1
b [%]	4.2 ± 2.2	7.5 ± 1.3
c [MeV]	71	72
χ^2/ndf	3.3/6	3.2/6

Table 12: Parameters of the energy resolution fits for the 2010 W-AHCAL π^-/π^+ data.

Figure 30: Energy resolution for the 2010 π^-/π^+ W-AHCAL data. The error bars are given by the quadratic sum of the statistical and systematic errors.

384 given in Table 11. The largest deviation is observed for the 10 GeV case, but the pion response is
 385 linear within statistical errors.

Runs	Noise RMS [MIPs]
Positive polarity	1.85 ± 0.02
Negative polarity	1.83 ± 0.03

Table 13: RMS of the energy distribution for randomly triggered events inside the beam spill, including all calorimeter layers.

Detector	Particle type	p_{beam}	a [%]	b [%]	c [MeV]	χ^2/ndf
Fe-AHCAL	π^+/π^-	10-80 GeV	57.6 ± 0.4	1.6 ± 0.3	180	50.4/14
DHCAL	π^+	3, 4, 8, 12, 20, 25 and 32 GeV	55.0 ± 0.6	0	74.8 ± 2.8	1.0/4
W-AHCAL	π^+	3-10 GeV	60.3 ± 1.1	7.5 ± 1.3	72	3.2/6

Table 14: Parameters of the π^+/π^- energy resolutions for the CALICE hadron calorimeters Fe-AHCAL [8], without software compensation, DHCAL [25] (for longitudinally contained pions) and W-AHCAL. In the Fe-AHCAL case, the noise term is the result of contributions for several detectors considered in the analysis: ECAL + HCAL + TCMT, where ECAL stands for Electromagnetic CALorimeter, and TCMT for Tail Catcher and Muon Tracker.

386 The energy resolution for π^-/π^+ data is shown in Fig. 30. The c -term is fixed to the spread (RMS)
 387 of the energy distribution in randomly triggered events inside the beam spill, considering all calorime-
 388 ter cells. The obtained values are given in Table 13.

389 The W-AHCAL π^+ energy resolution is compared to the other CALICE hadron calorimeters in
 390 Table 14. The Fe-AHCAL visible energy spectra are fitted with a Gaussian function in a ± 2 -RMS
 391 range around the mean value. For the DHCAL data, Gaussian fits of the full range were used.

392 The obtained constant term in the W-AHCAL case, which is similar to the value measured in
 393 the simulation (for QGSP_BERT_HP, $b = (10.3 \pm 0.1)\%$), may be higher than in the Fe-AHCAL
 394 case due to the fact that the analyzed energy range (from 3 to 10 GeV) is not large enough to impose
 395 reliable constraints on this term. This will be further investigated by the analysis of the high energy
 396 (10 GeV $< p < 300$ GeV) CERN 2011 data sample.

397 As the calorimeter response for π^+ and π^- is similar, the comparisons with simulation will be
 398 presented only for π^+ .

399 6.1 Calorimeter response

400 To quantify the agreement between simulation and data, we present the ratio between the mean
 401 visible energy in simulation and data, see Figs. 31 and 32.

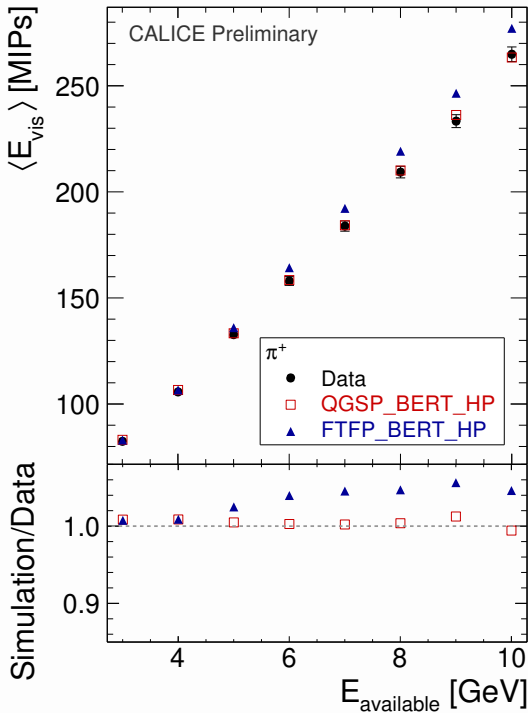


Figure 31: Mean π^+ visible energy: ratio between Bertini based simulations and data.

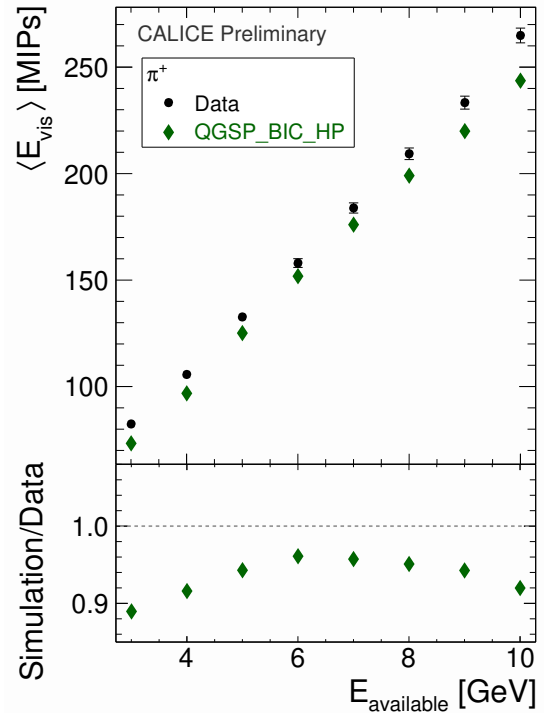


Figure 32: Mean π^+ visible energy: ratio between QGSP_BIC_HP and data.

402 The agreement with QGSP_BERT_HP is very good (at the level of 1%). As FTFP_BERT_HP
 403 shares the same model up to 5 GeV, the agreement is equally good, but the situation gets worse
 404 when switching to the FRITIOF model. For both Bertini based physics lists, a decrease of the
 405 energy ratio is observed for 10 GeV. This corresponds to the transition to the LEP model for
 406 QGSP_BERT_HP. On the other side, QGSP_BIC_HP shows a strong variation with the avail-
 407 able energy. The differences between data and the simulation are at the 10% level. However, as

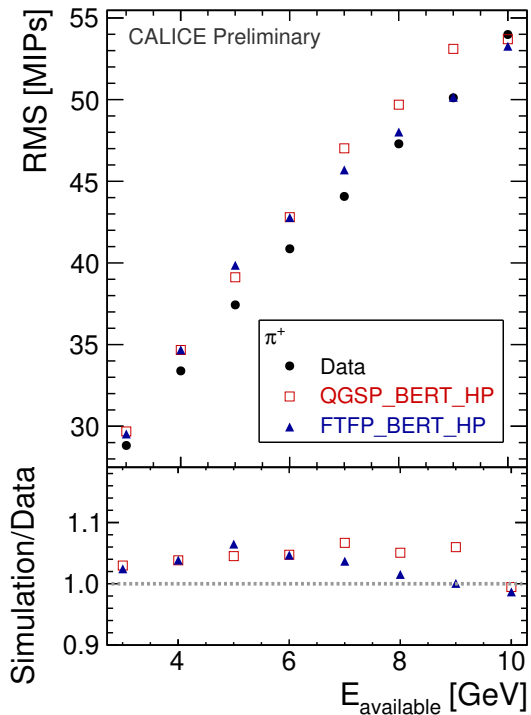


Figure 33: RMS of the visible energy vs. π^+ available energy: comparison of data with Bertini based physics lists.

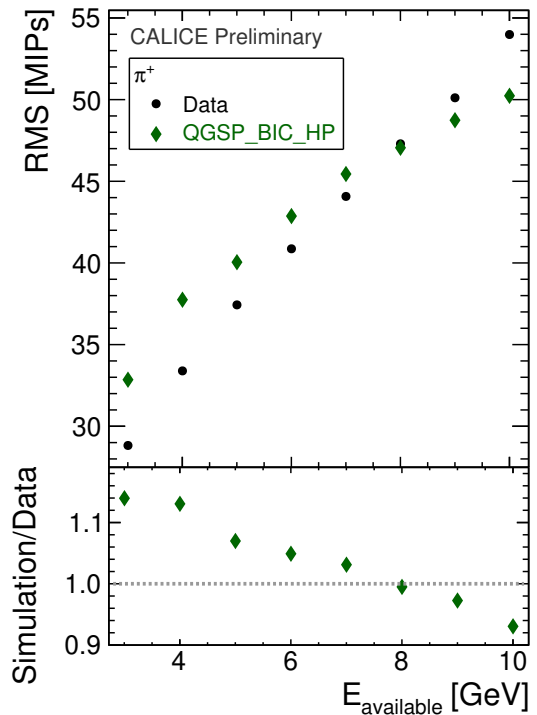


Figure 34: RMS of the visible energy vs. π^+ available energy: comparison of data with QGSP_BIC_HP physics list.

408 explained in Sect. 4.2, this list uses the LHEP parametrization for pions with $E_{\text{kin}} > 1.5$ GeV, and
 409 is presented here only for completeness.

410 The RMS of the visible energy distribution vs. pions' available energy, for the different physics
 411 lists, is shown in Figs. 33 and 34. For QGSP_BERT_HP, the agreement is within 5%. Contrary to
 412 observation at higher energies, the simulated distributions are in general somewhat broader than in
 413 data. FTFP_BERT_HP predicts better RMS for $E_{\text{available}} > 6$ GeV.

414 Example distributions of the visible energy are given in Figs. 35 and 36.

415 6.2 Longitudinal shower development

416 The longitudinal profiles for π^+ with three different beam momenta are compared with the
 417 QGSP_BERT_HP physics list in Figs. 37, 38 and 39. In general, the agreement is better than
 418 95%, with the exception of the first layer, where for all energies except 10 GeV, QGSP_BERT_HP
 419 predicts higher energy than observed in the data.

The distributions of the energy weighted layer number, defined as:

$$\text{E weighted layer number} = \frac{\sum_i E_i \cdot \text{layer}}{\sum_i E_i} \quad (6.10)$$

420 are shown for the 4 and 10 GeV cases in Figs. 40 and 41. The distributions are biased by the cut
 421 on the shower start, which is reflected in the knee at high values. However, data and simulation
 422 are biased in similar ways. The dependence of the mean energy weighted layer number on the

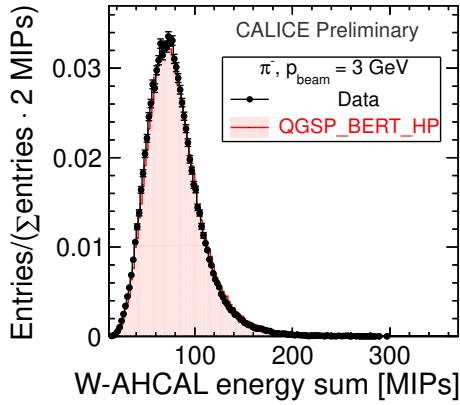


Figure 35: Energy sum distribution for π^+ with a beam momentum of 3 GeV: comparison of data with QGSP_BERT_HP.

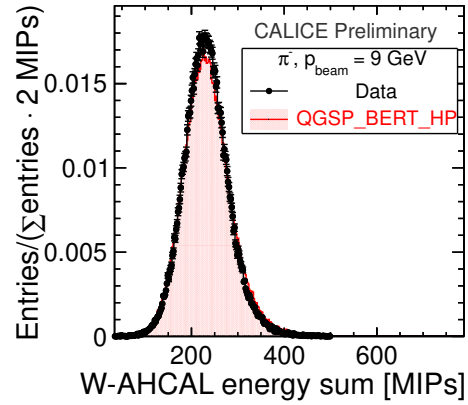


Figure 36: Energy sum distribution for π^+ with a beam momentum of 9 GeV: comparison of data with QGSP_BERT_HP.

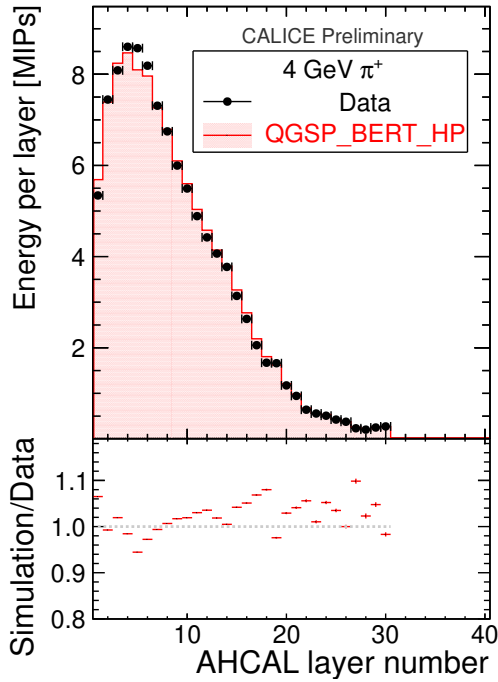


Figure 37: Longitudinal shower profile of π^+ with a beam momentum of 4 GeV: comparison of data with QGSP_BERT_HP.

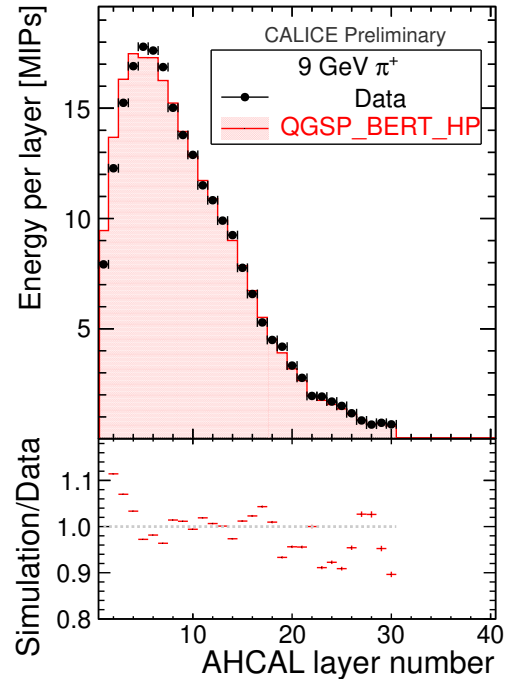


Figure 38: Longitudinal shower profile of π^+ with a beam momentum of 9 GeV: comparison of data with QGSP_BERT_HP.

423 available energy is presented in Fig. 42, which contains also the ratio between the simulation and
 424 data. The observed agreement is within 3%.

425 7. Analysis of the proton data

426 In a first approach, one expects the calorimeter response to be similar for pions and protons. How-

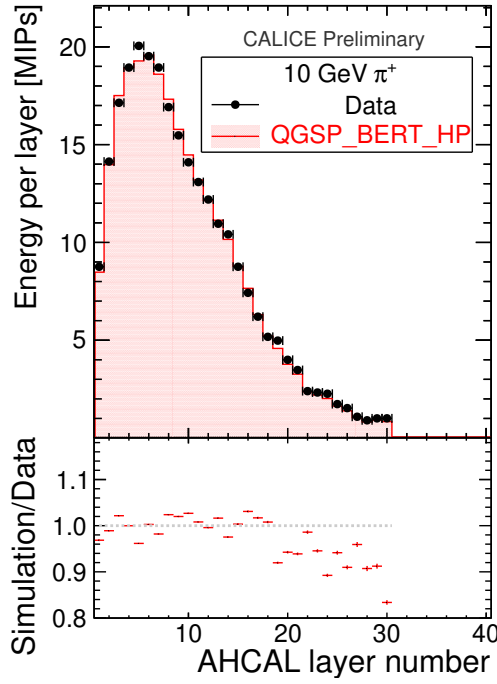


Figure 39: Longitudinal shower profile of π^+ with a beam momentum of 10 GeV: comparison of data with QGSP_BERT_HP.

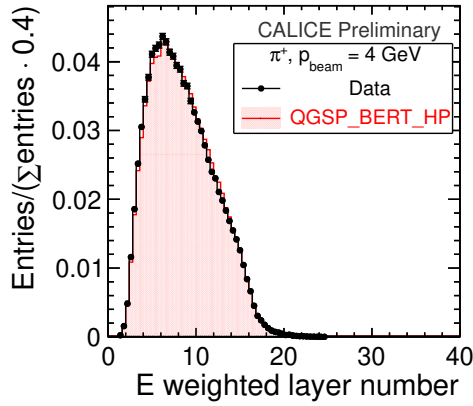


Figure 40: Distribution of the energy weighted layer number of π^+ with a beam momentum of 4 GeV: comparison of data with QGSP_BERT_HP.

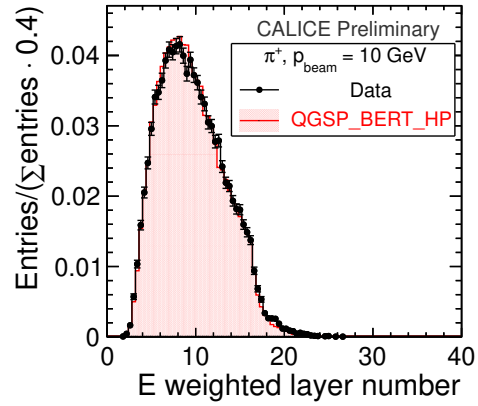


Figure 41: Distribution of the energy weighted layer number of π^+ with a beam momentum of 10 GeV: comparison of data with QGSP_BERT_HP.

427 ever, there are differences mainly due to two effects [27]:

- The first effect is due to the differences in the energy available for deposition in calorimeter. For pions, it is given in Eq. 6.9. As protons do not decay, the energy is:

$$E_{\text{available}} = E_{\text{kin}} = \sqrt{p_{\text{beam}}^2 + m_{\text{proton}}^2} - m_{\text{proton}}, \quad (7.1)$$

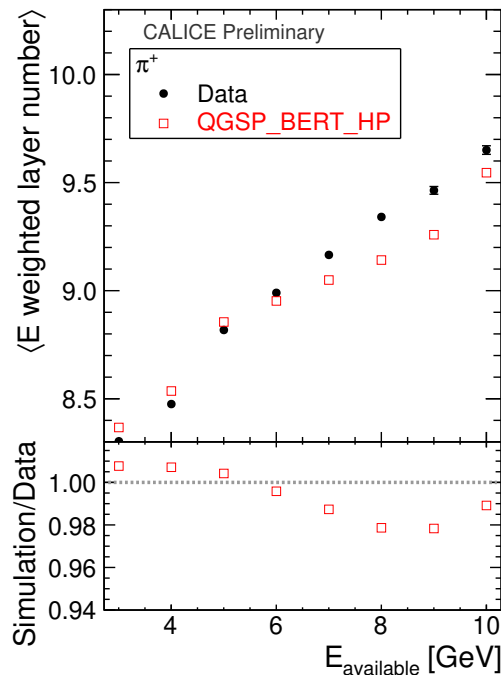


Figure 42: Dependence of the mean energy weighted layer number of π^+ initiated showers on the available energy: comparison of data with QGSP_BERT_HP. One layer corresponds to $0.13 \lambda_l$ (Table 1). In the lower part, the ratio between simulation and data is shown.

428 where $m_{\text{proton}} = 938.27$ MeV is the proton mass. This is relevant for the low energy range
 429 analyzed in this note.

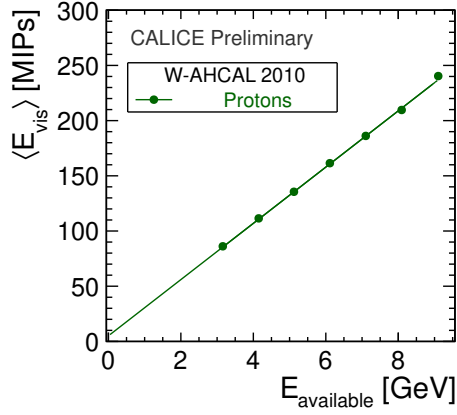
- 430 • The second effect originates from the different fractions of π^0 mesons produced in protons
 431 versus pion induced showers. As a consequence of the baryon number conservation, which
 432 favors the production of leading baryons, one expects a smaller average number of π^0 mesons
 433 in proton showers, compared to pion showers. In the latter case, the leading particle may be
 434 a π^0 [28], due to the charge exchange reaction⁸: $\pi^+ + n \rightarrow \pi^0 + p$. A smaller number
 435 of π^0 implies a smaller electromagnetic fraction in the shower. For a non-compensating
 436 calorimeter ($el/h > 1$), this results in a higher response for pions than for protons.

437 The selection for protons is the same as for pions, see Sect. 6, apart from the Cherenkov-based
 438 selection. Only runs with beam momenta from 4 to 10 GeV are included for the proton analysis.
 439 Due to non-optimized pressures, the Cherenkov triggers were inefficient for $p_{\text{beam}} < 4$ GeV, the
 440 sample containing also a sizable fraction of pions in addition to protons and muons. In a future
 441 analysis one might consider possibilities of reducing the pion contamination.

442 7.1 Calorimeter response

443 The average calorimeter response for protons vs. the available beam energy is shown in Fig. 43,

⁸This reaction is favoured by the large number of neutrons in tungsten, which has about 50% more neutrons than protons.



Parameter	Protons
u [MIPs]	5.03 ± 2.24
v [MIPs/GeV]	25.48 ± 0.43
χ^2/ndf	1.4/5

Table 15: Fit parameters of the dependence of the mean proton visible energy on the available energy.

Figure 43: Dependence of the mean visible proton energy $\langle E_{\text{rec}} \rangle$ on the available energy. The error bars are given by the quadratic sum of the statistical and systematic errors. The lines indicate fits with the function $\langle E_{\text{vis}} \rangle = u + v \cdot E_{\text{available}}$.

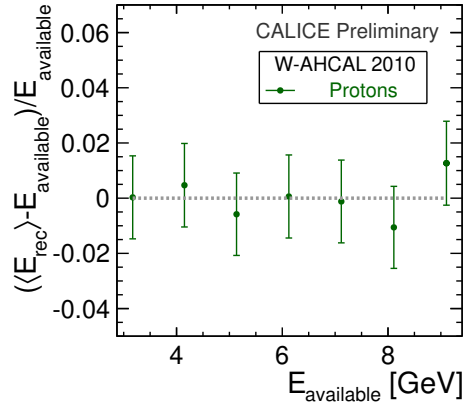


Figure 44: Deviations from linearity for the W-AHCAL 2010 proton data.

444 while the deviations from linearity are displayed in Fig. 44. The proton response is linear within
 445 the errors.

446 The corresponding energy resolution, obtained using Eq. 6.8, is presented in Fig. 45. The
 447 noise term is fixed to the same value as for the π^+ data (Table 13). The fitting function is given by
 448 Eq. 5.4.

449 The obtained resolution of $61.9\%/\sqrt{E}$ is comparable with the pion case ($60.3\%/\sqrt{E}$), the
 450 main difference is the constant term, which is slightly higher: 11.3% for protons, compared to
 451 7.5% for pions. This is compatible with expectations from simulation. QGSP_BERT_HP and
 452 FTFP_BERT_HP predict a stochastic term of about 59%, and a constant term of about 13~14%.

453 The visible energy for electrons, pions and protons is shown vs. their available energy in
 454 Fig. 46. The e^+ data has a slope slightly different from hadrons, but the calorimeter response is

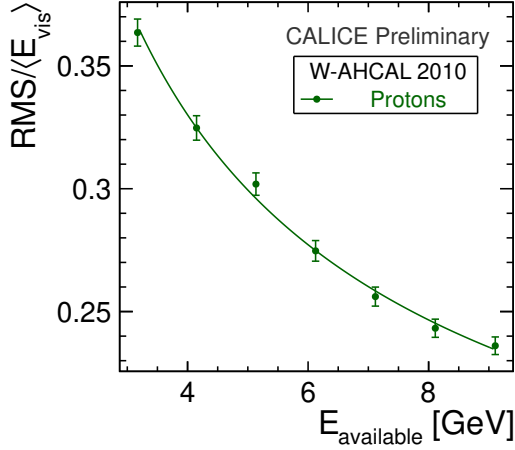


Figure 45: Fit of the proton energy resolution defined as $\text{RMS}/\langle E_{\text{vis}} \rangle$. The error bars are given by the quadratic sum of the statistical and systematic errors.

Parameter	Proton
a [%]	61.9 ± 1.3
b [%]	11.3 ± 1.2
c [MeV]	73
χ^2/ndf	2.8/5

Table 16: Parameters of the proton energy resolution fit.

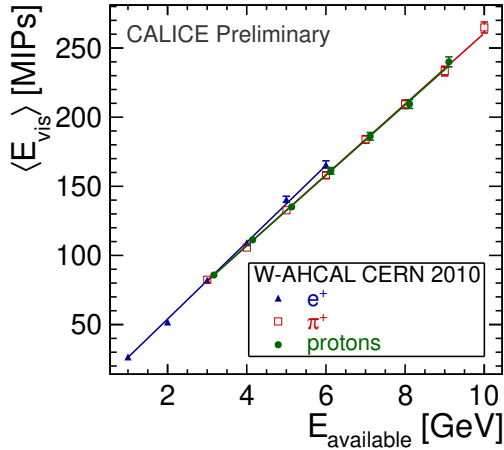


Figure 46: Dependence of the mean visible energy ($\langle E_{\text{rec}} \rangle$) on the available energy for the particles analyzed in this paper. This is a summary of the results shown in Figs. 15, 28 and 43. In the e^+ case, the mean energy is obtained from a fit, while for hadrons it is given by the statistical mean of the corresponding distribution. The error bars are given by the quadratic sum of the statistical and systematic errors.

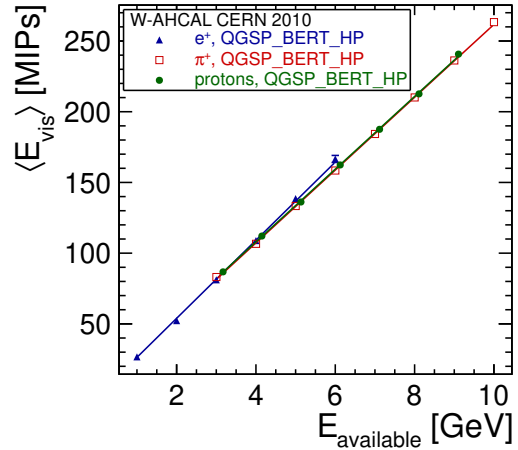


Figure 47: Dependence of the **simulated** mean visible energy ($\langle E_{\text{rec}} \rangle$) on the available energy for the particles analyzed in this paper. The QGSP_BERT_HP physics list was used for the simulation. In the e^+ case, the mean energy is obtained from a fit, while for hadrons it is given by the statistical mean of the corresponding distribution.

455 similar for all three particle types in the analyzed low energy range. This is also predicted by the
 456 simulation (shown in Fig. 47). It should be noted that in the e^+ case, the mean energy is obtained
 457 from a fit with the Novosibirsk function, while for hadrons it is given by the statistical mean of the

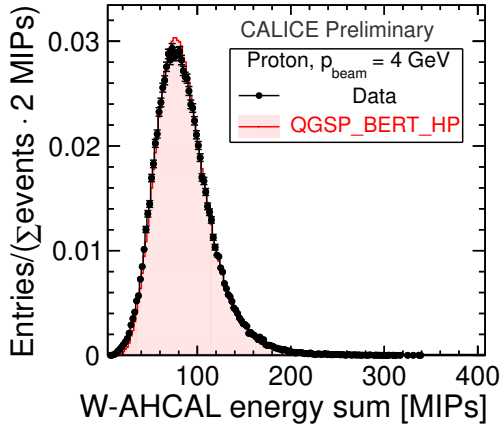


Figure 48: The visible energy distribution of a proton with a beam momentum of 4 GeV: comparison of data with QGSP_BERT_HP.

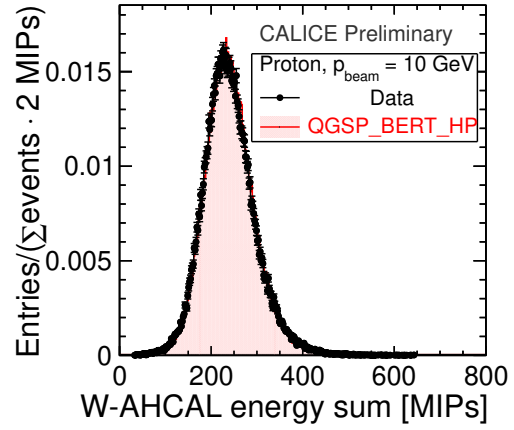


Figure 49: The visible energy distribution of a proton with a beam momentum of 10 GeV: comparison of data with QGSP_BERT_HP.

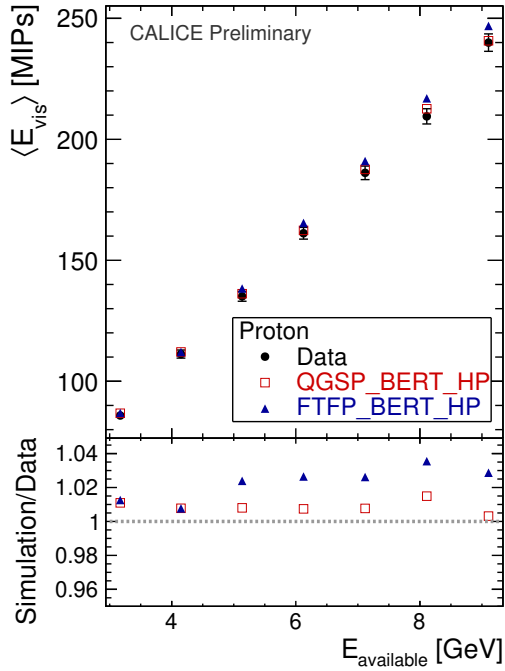


Figure 50: Proton visible energy: ratio between Bertini based physics lists and data.

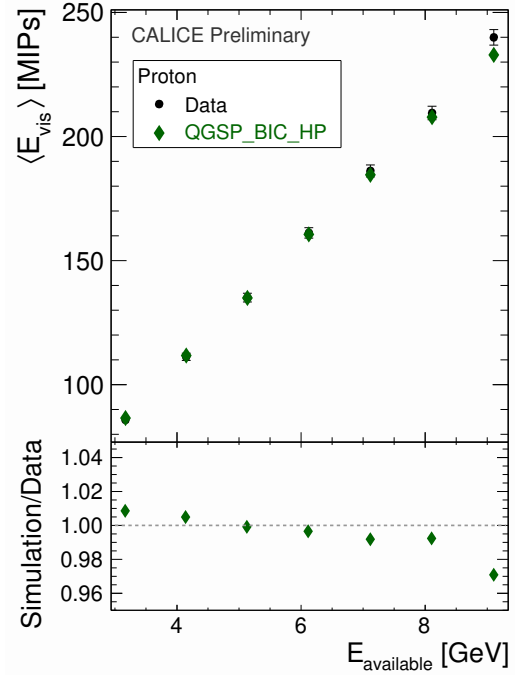


Figure 51: Proton visible energy: ratio between QGSP_BIC_HP and data.

458 corresponding distribution. However, it was checked that the mean from the Novosibirsk fit is very
 459 similar to the statistical mean of the distribution (Appendix D).

460 The proton visible energy distribution is compared to the QGSP_BERT_HP physics list in
 461 Fig. 48 for the 4 GeV case, and in Fig. 49 for 10 GeV. The level of agreement between data and sim-
 462 ulation is very good. It is quantified by the response ratio shown in Fig. 50 for the selected Bertini
 463 based physics lists, and in Fig. 51 for QGSP_BIC_HP. As in the pion case, QGSP_BERT_HP per-

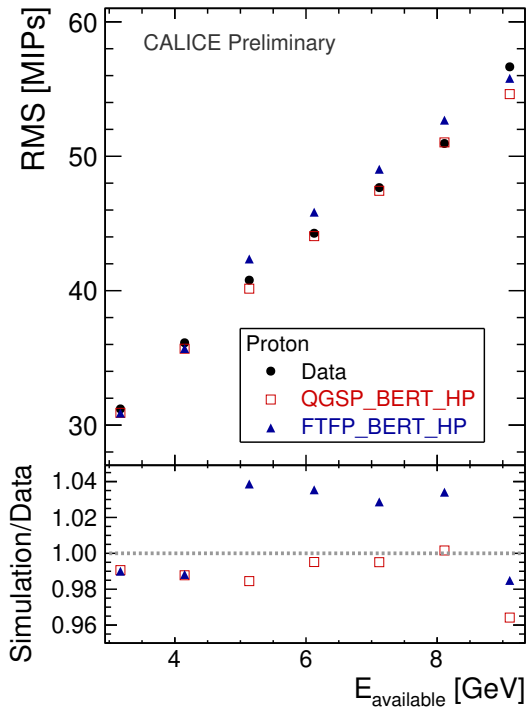


Figure 52: RMS of proton visible energy distribution: comparison of data with Bertini based physics lists.

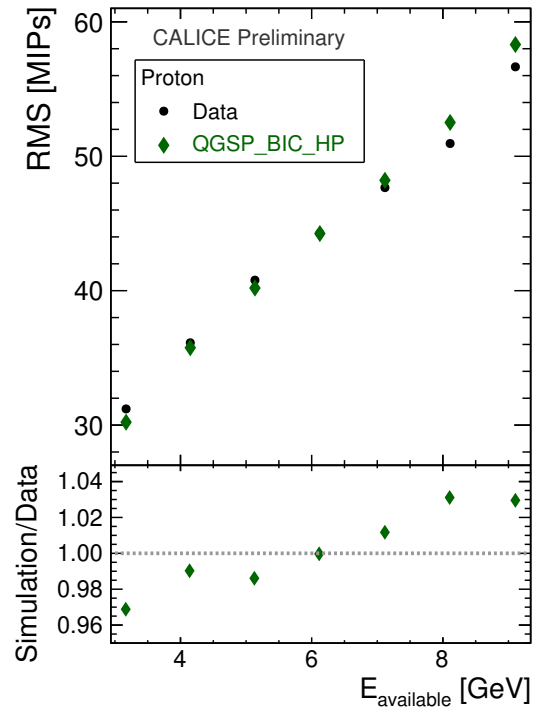


Figure 53: RMS of proton visible energy distribution: comparison of data with QGSP_BIC_HP.

464 forms very well, the differences being less than 2%. For protons, QGSP_BIC_HP performs also
 465 well, although there is a dependence on the available energy. As explained in Sect. 4.2, here the
 466 Binary Cascade model is applied for energies up to 9 GeV, afterwards the transition is done to the
 467 LEP model. The same dependence of QGSP_BIC_HP on the available energy is observed for the
 468 RMS of the energy distribution (see Fig. 52 compared to Fig. 53), but the agreement is within 4%.

469 **7.2 Longitudinal shower development**

470 The longitudinal shower profiles for protons with beam momenta with 4 and 10 GeV are presented
 471 for QGSP_BERT_HP and QGSP_BIC_HP in Figs. 54 to 57. QGSP_BERT_HP performs well over
 472 the analyzed energy range, while for $p_{\text{beam}} > 4$ GeV the Binary cascade model predicts a somewhat
 473 later shower maximum than in data, and a reduced response in the first calorimeter part.

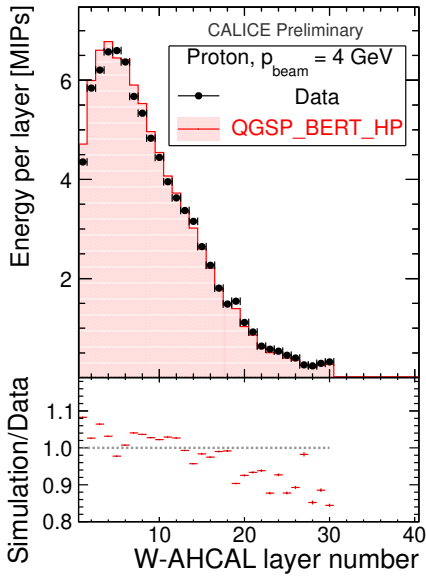


Figure 54: Longitudinal shower profile for a proton with a beam momentum of 4 GeV: comparison of data with QGSP_BERT_HP.

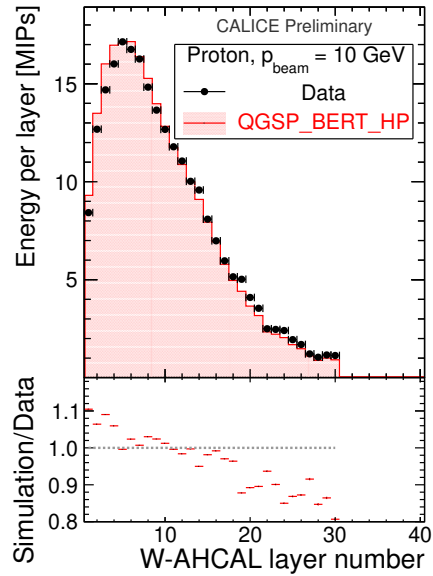


Figure 55: Longitudinal shower profile for a proton with a beam momentum of 10 GeV: comparison of data with QGSP_BERT_HP.

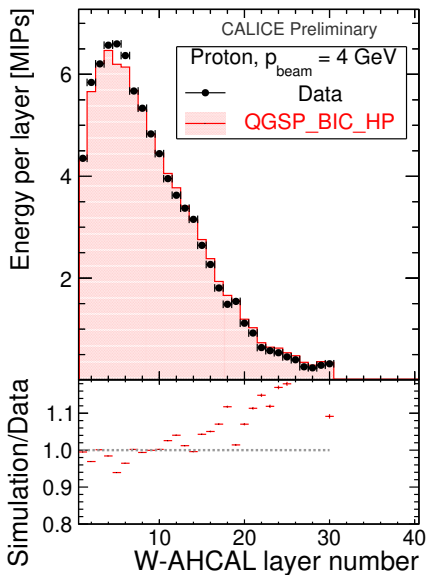


Figure 56: Longitudinal shower profile for a proton with a beam momentum of 4 GeV: comparison of data with QGSP_BIC_HP.

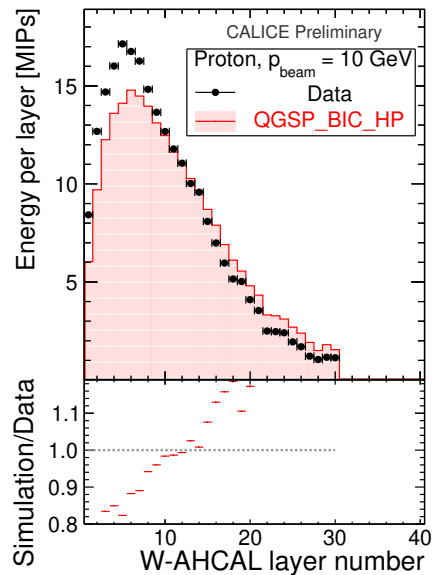


Figure 57: Longitudinal shower profile for a proton with a beam momentum of 10 GeV: comparison of data with QGSP_BIC_HP.

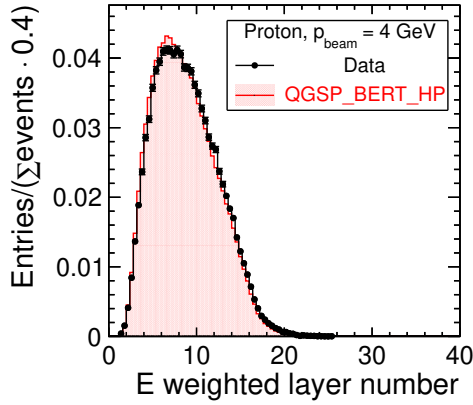


Figure 58: Distribution of the energy weighted layer number for a proton with a beam momentum of 4 GeV: comparison of data with QGSP_BERT_HP.

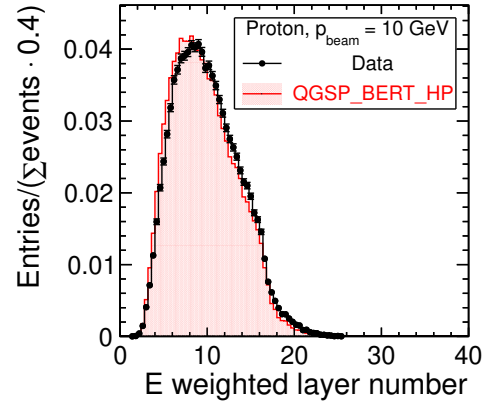


Figure 59: Distribution of the energy weighted layer number for a proton with a beam momentum of 10 GeV: comparison of data with QGSP_BERT_HP.

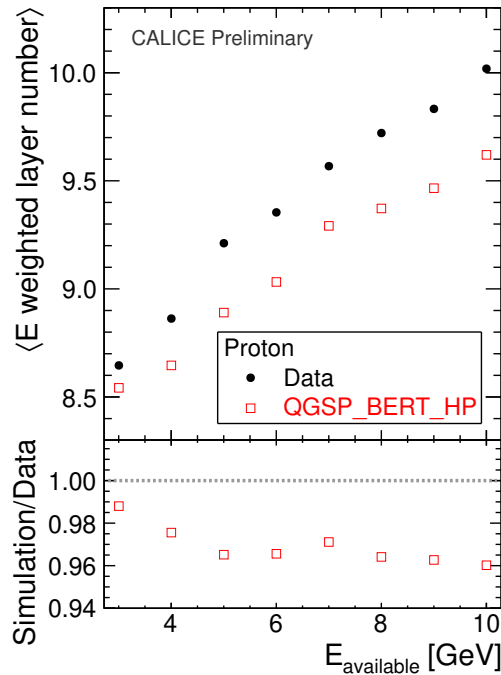


Figure 60: Dependence of the mean energy weighted layer number for proton initiated showers vs. the available energy: comparison of data with QGSP_BERT_HP. One layer corresponds to $0.13 \lambda_l$ (Table 1). In the lower part, the ratio between simulation and data is shown.

474 The distributions of the energy weighted layer number (defined in Eq. 6.10) for protons with
 475 beam momenta of 4 and 10 GeV are shown in Fig. 58 and 59. The dependence of the mean energy
 476 weighted layer number on the available energy is presented in Fig. 60, together with the ratio
 477 between QGSP_BERT_HP and data. This GEANT4 physics list predicts showers at slightly smaller

478 energy weighted layer numbers than in data, but the differences are within 4%.

479 **8. Summary and conclusions**

480 We presented a first study of low momentum ($p \leq 10$ GeV) electron, pion and proton initiated
481 showers in the CALICE tungsten-scintillator AHCAL. The analysis includes measurements of the
482 energy resolution for the different particle types and studies of the shower development in the lon-
483 gitudinal plane. The obtained energy resolution for hadrons has a stochastic term of approximately
484 $60\%/\sqrt{E}$.

485 The modeling of the detector configuration and response is verified with electrons and shows
486 excellent agreement with data.

487 The results are compared with the GEANT4 physics lists: QGSP_BERT_HP,
488 FTFP_BERT_HP and QGSP_BIC_HP. The first physics list is found to perform remarkably well
489 for both pions and protons, the agreement being for most of the studied variables within 3% or
490 better. In case of protons, QGSP_BIC_HP does not only reasonably describe the average calorime-
491 ter response, but also the width of the visible energy distribution. We found indications that the
492 addition of the data driven High Precision neutron package is relevant for particle interactions in
493 dense materials like tungsten, where neutrons are expected to play a role.

494 We observed that the CALICE W-AHCAL response to electrons, pions and protons is very
495 similar in the analyzed low energy range. This will be further studied in the future, by including
496 the high energy data ($10 \text{ GeV} < p < 300 \text{ GeV}$) collected at the CERN SPS in 2011.

497 **A. List of selected runs**

Energy	Run number	
	Negative polarity	Positive polarity
1	360583 360584	360629 360629
2	360782 360785	360550, 360551 360552, 360573 360810, 360811
3	360835 360836	360598, 360599 360615, 360616
4	360774	360536, 360543 360570, 360571 360801, 360802
5	360827 360834	360591, 360597 360613, 360614
6	360707 360771 360772	360533, 360534 360617, 360618 360563, 360564 360799, 360800
7	360825 360826	360589, 360590 360611, 360612 360644, 360645
8	360767 360770	360532, 360561 360626, 360627 360633, 360796 360797
9	360823 360824	360619, 360642 360643, 360837 360838
10	360646 360647	360640, 360641 360786, 360795

Table 17: List of selected runs from the 2010 CALICE W-AHCAL data taking. Each run has approximately 150000 events.

498 **B. Cross-talk factor**

499 To account for the light leakage between the tiles, a so-called **cross-talk factor** is introduced in
 500 digitization. The default value for this factor is 10%, i.e. 2.5% per tile edge. As explained in [5],
 501 this value was measured for two tiles, and it was found to give satisfactory agreement between data
 502 and simulation.

503 In Fig. 61 the ratio of the positron visible energy between simulation and data, using a cross-
 504 talk factor of 10% and a MIP to GeV factor of 816 keV is shown. An example of the longitudinal
 505 profile of a 3 GeV positron is shown in Fig. 62. The agreement between data and the simulation
 506 digitized using these factors is very good.

507 However, the MIP to GeV factor was meanwhile changed from 816 keV to 805 keV. The
 508 distribution of the energy deposited by a simulated muon in is fitted with a Landau function. Nev-
 509 ertheless, the resulting most probable value does not correspond to the exact position of the peak
 510 maximum, but for numerical reasons it includes a shift [30]. The new value of the MIP to GeV
 511 factor takes this shift into consideration.

512 While using this new value of the MIP to GeV factor (of 805 keV), the default cross-talk
 513 factor of 10% gives a systematically higher energy in simulation, by about 2-3%, as can be seen in
 514 Figs. 63 and 64.

515 Better results are obtained using a cross-talk factor of 8%, as shown in Figs. 65 and 66. There-
 516 fore, for the W-AHCAL simulation, a cross-talk factor of 8% and a MIP to GeV factors of 805 keV
 517 are used, which is overall consistent with the values used in [5].

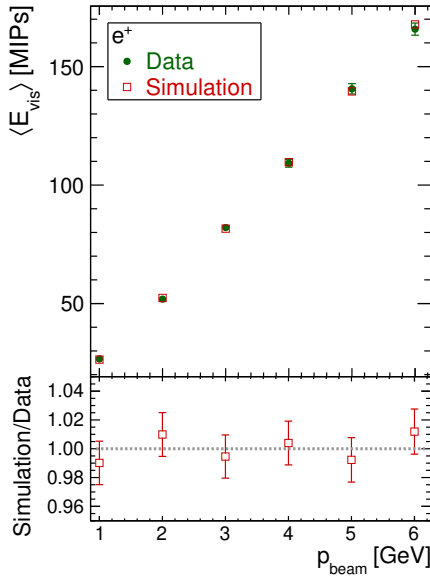


Figure 61: Ratio of the positron visible energy between simulation and data. In digitization, a cross-talk factor of 10%, and a MIP to GeV factor of 816 keV were used.

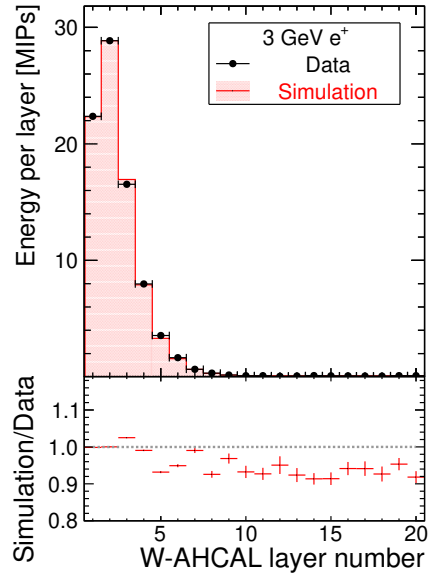


Figure 62: Longitudinal profile for a 3 GeV positron: comparison of data with simulation, for which a cross-talk factor of 10% and a MIP to GeV factor of 816 keV were used.

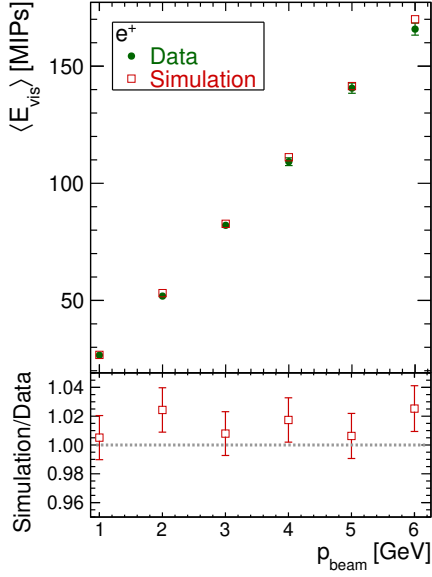


Figure 63: Ratio of the positron visible energy between simulation and data. In digitization, a cross-talk factor of **10%**, and a MIP to GeV factor of **805 keV** were used.

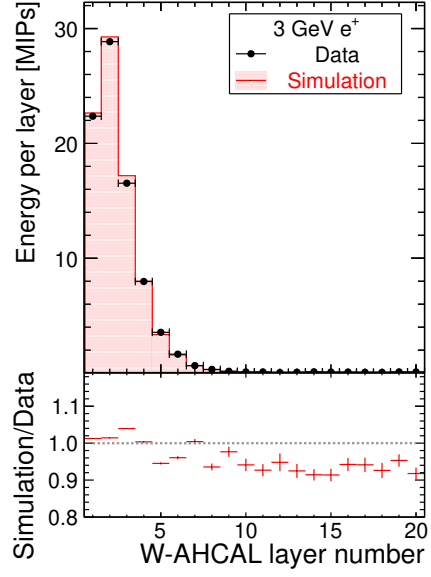


Figure 64: Longitudinal profile for a 3 GeV positron: comparison of data with simulation, for which a cross-talk factor of **10%** and a MIP to GeV factor of **805 keV** were used.

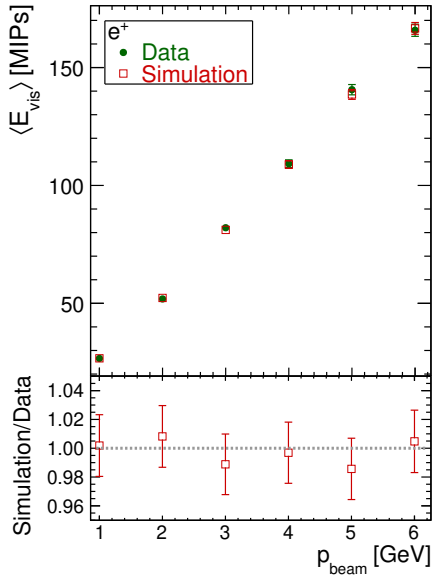


Figure 65: Ratio of the positron visible energy between simulation and data. In digitization, a cross-talk factor of **8%**, and a MIP to GeV factor of **805 keV** were used.

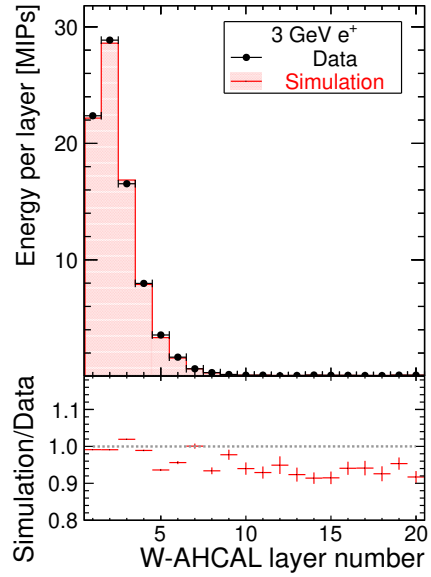


Figure 66: Longitudinal profile for a 3 GeV positron: comparison of data with simulation, for which a cross-talk factor of **8%** and a MIP to GeV factor of **805 keV** were used.

C. Electromagnetic energy distributions and Novosibirsk fits

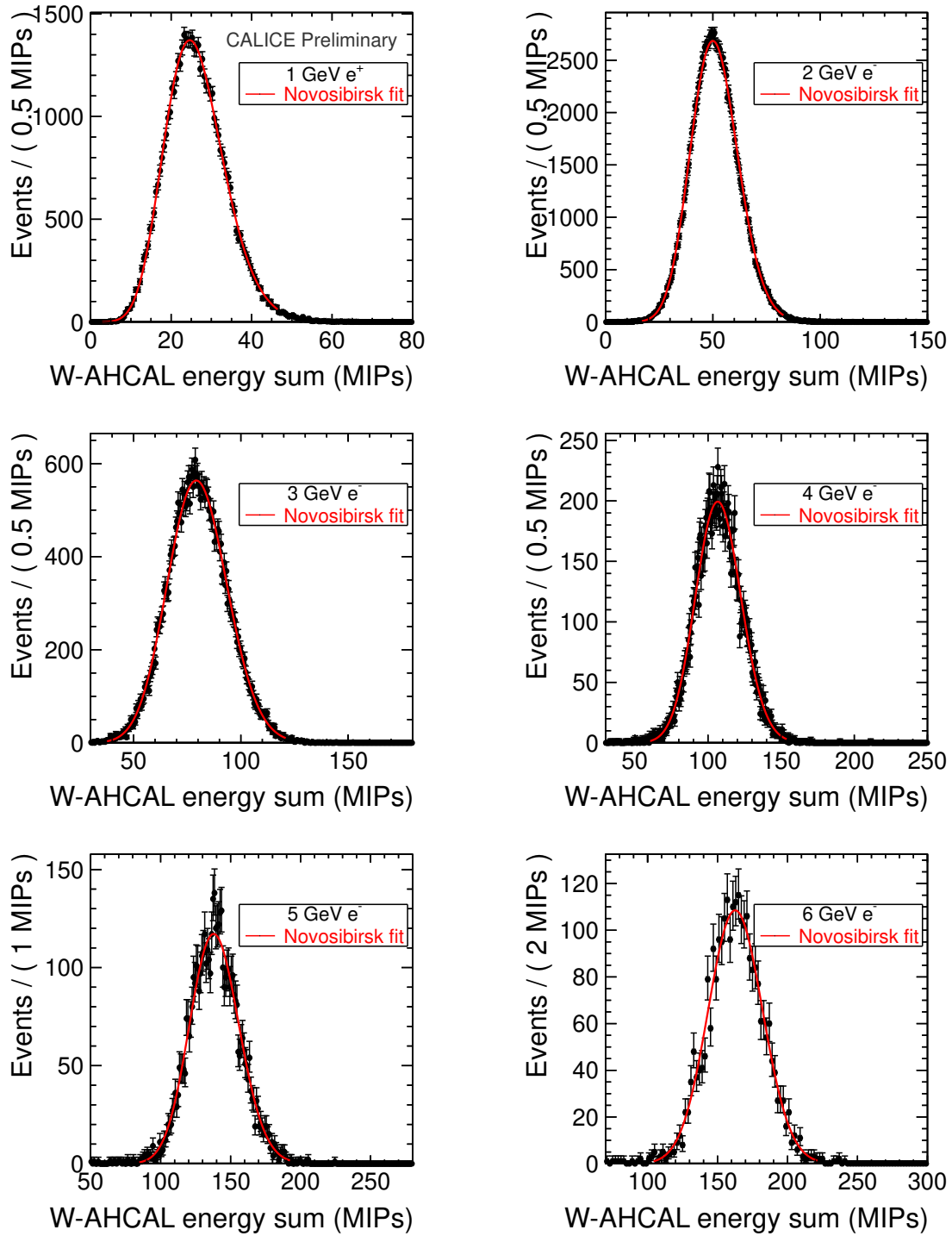


Figure 67: Fits with the Novosibirsk function of the visible energy in showers initiated by positrons with energies from 1 to 6 GeV.

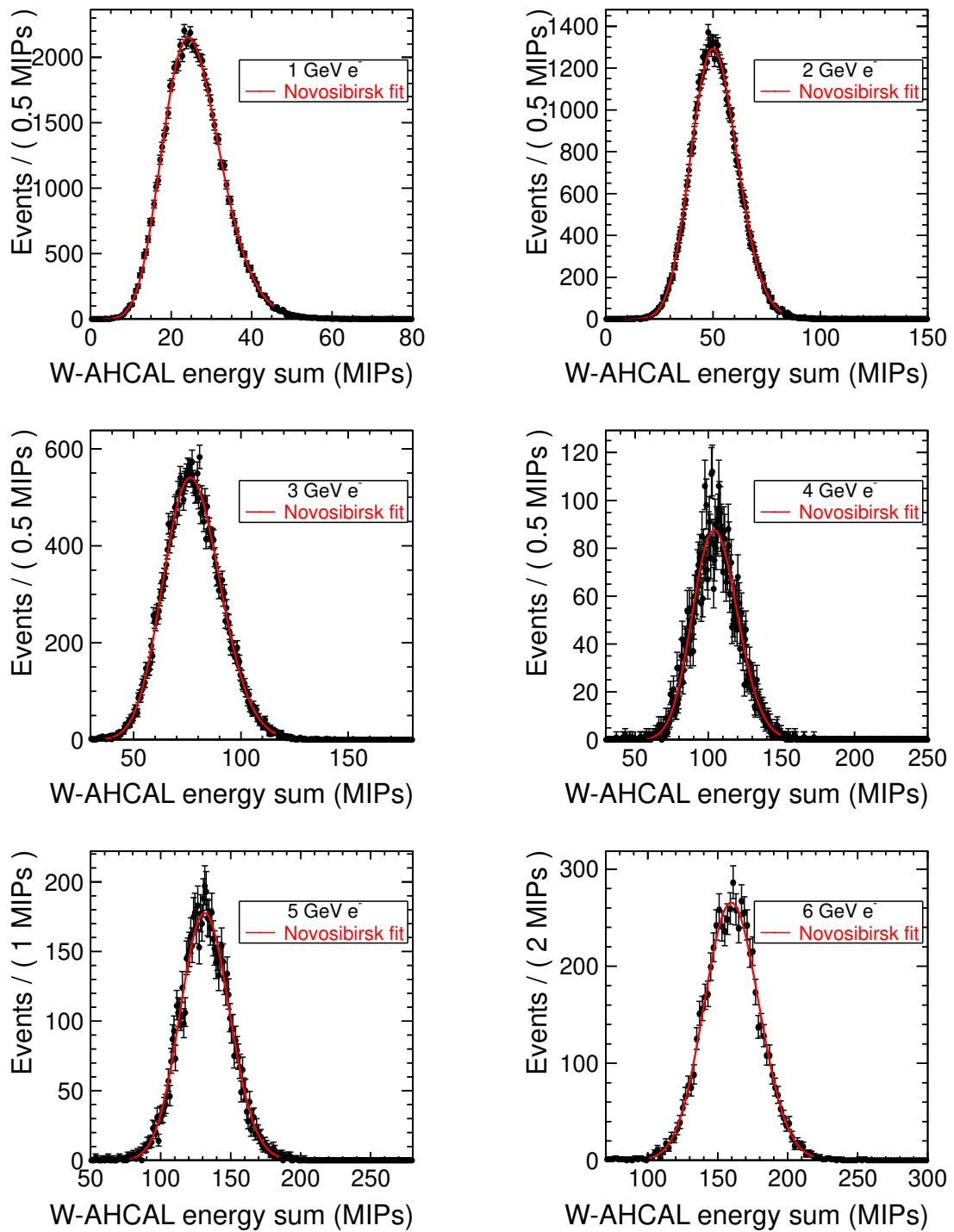


Figure 68: Fits with the Novosibirsk function of the visible energy in showers initiated by electrons with energy from 1 to 6 GeV.

p_{beam}	Particle	Mean (μ)	σ	Tail (τ)	χ^2/ndf
1 GeV	e^+	26.62 ± 0.06	7.43 ± 0.03	0.150 ± 0.005	1.35
	e^-	25.93 ± 0.05	7.21 ± 0.04	0.146 ± 0.004	0.94
2 GeV	e^+	51.86 ± 0.05	11.11 ± 0.02	0.069 ± 0.003	1.59
	e^-	51.77 ± 0.07	10.88 ± 0.03	0.075 ± 0.004	1.16
3 GeV	e^+	82.06 ± 0.12	14.06 ± 0.05	0.047 ± 0.005	1.03
	e^-	78.77 ± 0.12	13.39 ± 0.05	0.068 ± 0.005	0.94
4 GeV	e^+	109.22 ± 0.21	15.61 ± 0.10	0.040 ± 0.008	0.76
	e^-	106.86 ± 0.32	15.37 ± 0.14	0.050 ± 0.012	0.81
5 GeV	e^+	140.61 ± 0.57	17.84 ± 0.27	0.043 ± 0.018	0.77
	e^-	134.29 ± 0.33	17.55 ± 0.15	0.031 ± 0.011	0.98
6 GeV	e^+	165.81 ± 0.64	19.61 ± 0.29	0.024 ± 0.019	0.90
	e^-	162.83 ± 0.41	19.53 ± 0.18	0.030 ± 0.012	0.85

Table 18: Novosibirsk fit results for the 2010 W-AHCAL e^+/e^- data.

519 **D. Comparison of methods to measure electromagnetic energy resolution**

520 This section presents a comparison of the electromagnetic energy resolution obtained using the
 521 Novosibirsk fit function, and Gaussian fits in a range containing 80% of the statistics, with respect
 522 to the median of the histogram.

523 The individual fit results using the Novosibirsk function can be found in Appendix C. In
 524 Fig. 69 the Gaussian fits are shown for the e^+ data.

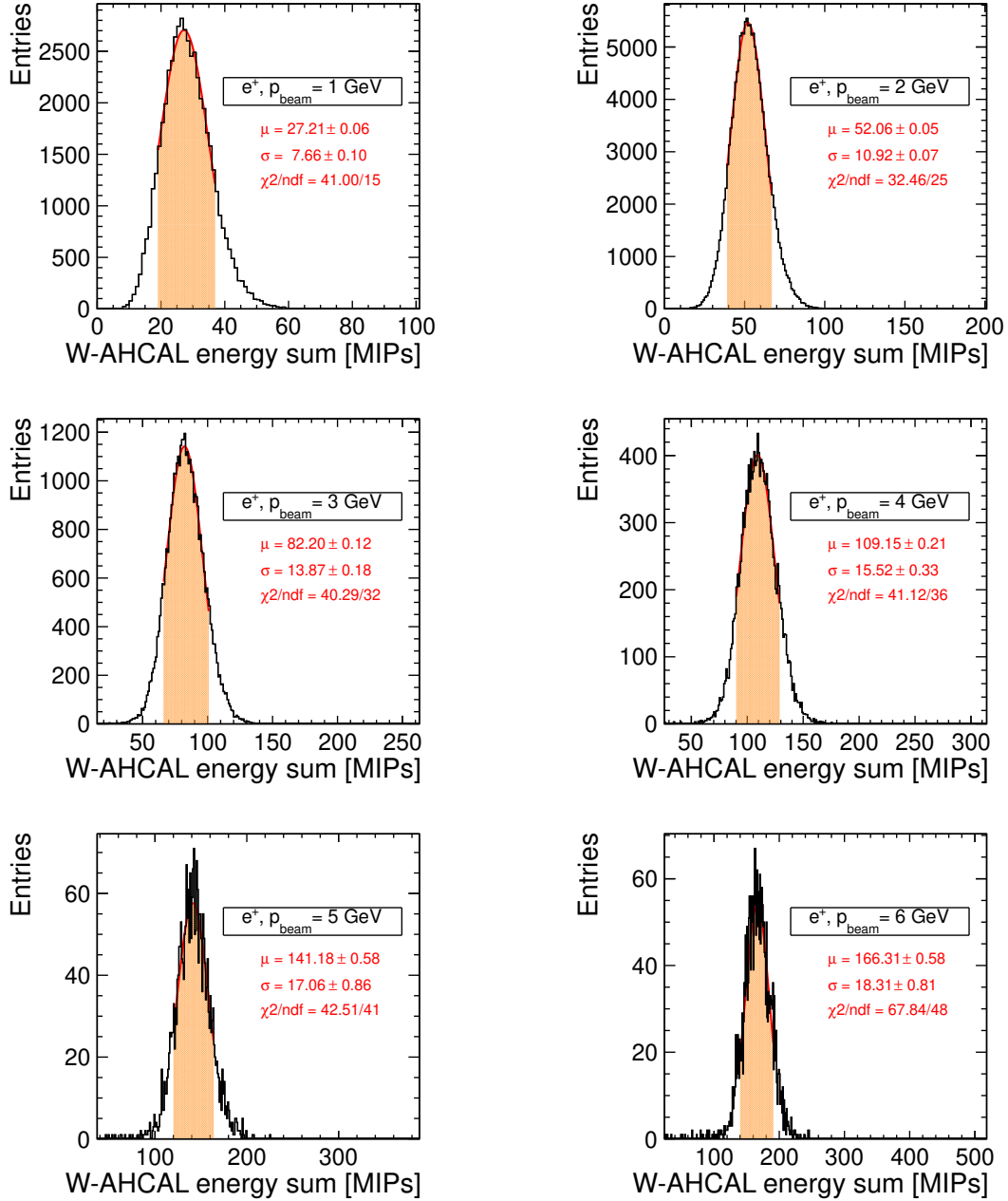


Figure 69: Gaussian fits of the visible energy in showers initiated by positrons with energies from 1 to 4 GeV. The fit region is defined to contain 80% of the statistics, with respect to the median of the histogram.

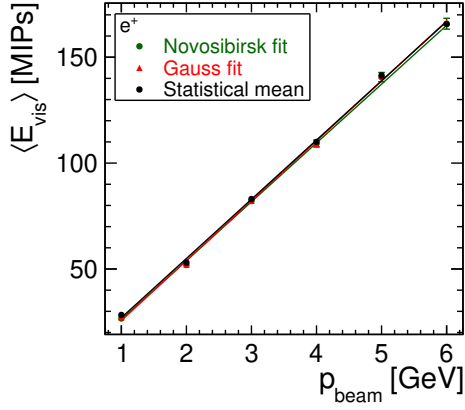


Figure 70: Dependence of the positron visible energy on the beam momenta: comparison of methods. The errors are given by the quadratic sum of statistical and systematic errors. The lines indicate a fit with the function $\langle E_{\text{vis}} \rangle = u + v \cdot p_{\text{beam}}$.

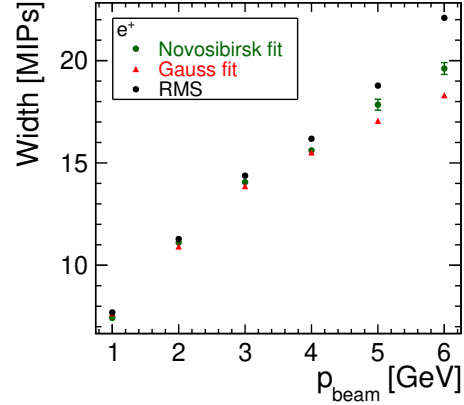


Figure 71: Width of the positron visible energy distribution vs. beam momenta: comparison of methods.

Parameter	Method		
	Novosibirsk	Gaussian	RMS
u [MIPs]	-1.56 ± 0.58	-2.63 ± 1.75	-0.96 ± 1.75
v [MIPs/GeV]	27.77 ± 0.30	28.28 ± 0.45	27.96 ± 0.45
χ^2/ndf	11.0/4	14.1/4	14.2/4

Table 19: Fit parameters of the dependence of the mean e^+ visible energy on the beam momenta: comparison of methods.

525 In order to be able to compare the e^+ calorimeter response to the hadrons' response, the de-
526 pendence of the mean visible energy on the beam momenta is shown using also the statistical mean
527 of the histogram in Fig. 70. The corresponding fit results are given in Table 19.

528 The width of the visible energy distribution, obtained with the different methods, is displayed
529 in Fig. 71. As the number of events decreases significantly with increasing energy, the statistical
530 RMS differs more and more from the values obtained with the considered fit methods, therefore it
531 is not considered in the energy resolution fits shown in Fig. 72.

532 The results of the energy resolution fits are presented in Table 20. The two fits give similar
533 energy resolutions, within the errors.

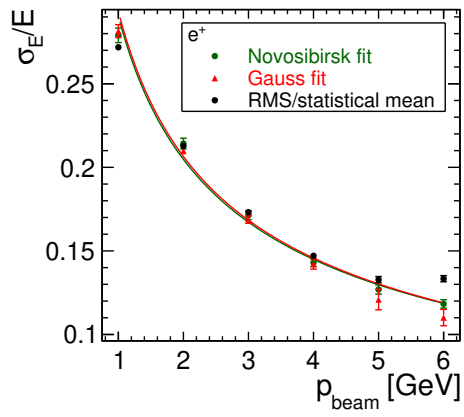


Figure 72: Positron energy resolution: comparison of methods. The errors are given by the quadratic sum of statistical and systematic errors.

Parameter	Fit	
	Novosibirsk	Gaussian
a [%]	28.7 ± 0.4	29.1 ± 0.2
b [%]	1.6 ± 2.3	0 ± 1.7
c [MeV]	38	37
χ^2/ndf	19.6/4	22.0/4

Table 20: Fit parameters of the e^+ energy resolution: comparison of methods.

534 **E. Selection of hadron events**

535 The effect of the cuts used to reduce the fraction of muon and late showering hadrons in the number
 536 of hits vs. z_{cog} distribution is shown for π^+ data with beam momenta of 3 and 10 GeV in Figs. 73,
 537 74, 75 and 76. The z_{cog} variable is defined in Eq. 5.1.

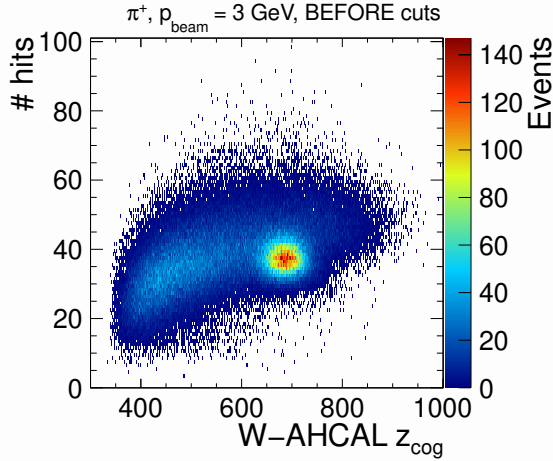


Figure 73: Data: Distribution of the number of hits vs. z_{cog} for showers generated by a π^+ with a beam momentum of 3 GeV, **before** applying the cuts for hadron selection.

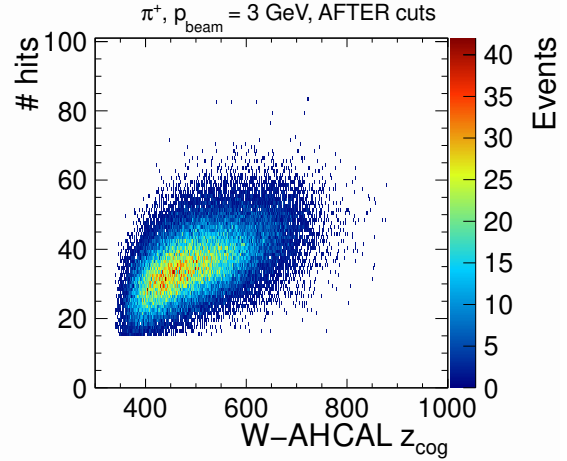


Figure 74: Data: Distribution of the number of hits vs. z_{cog} for showers generated by a π^+ with a beam momentum of 3 GeV, **after** applying the cuts for hadron selection.

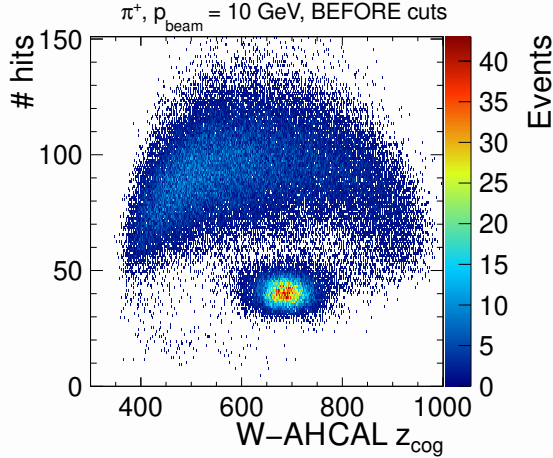


Figure 75: Data: Distribution of the number of hits vs. z_{cog} for showers generated by a π^+ with a beam momentum of 10 GeV, **before** applying the cuts for hadron selection.

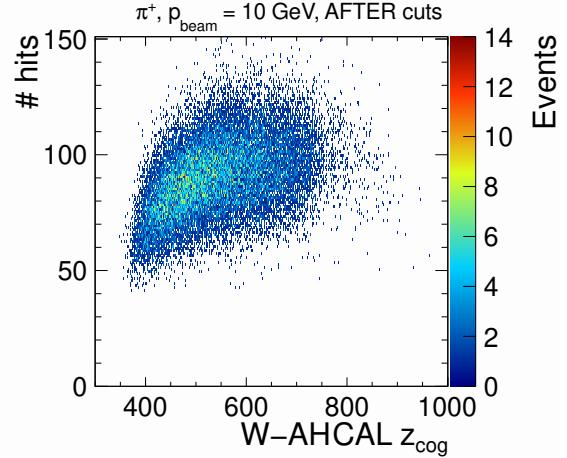


Figure 76: Data: Distribution of the number of hits vs. z_{cog} for showers generated by a π^+ with a beam momentum of 10 GeV, **after** applying the cuts for hadron selection.

538 For a qualitative comparison, the effect of the applied cuts in simulation is shown in Figs. 77
 539 to 80, for the QGSP_BERT_HP physics list.

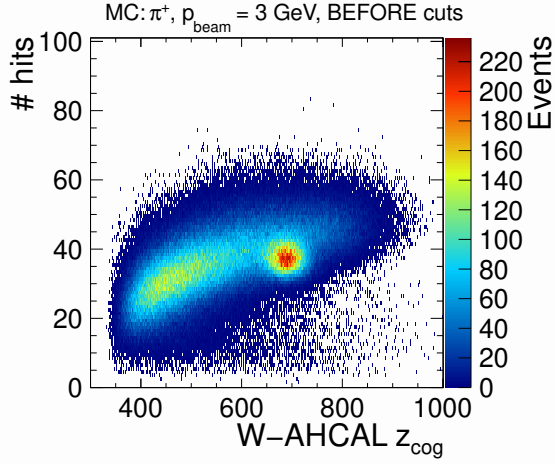


Figure 77: QGSP_BERT_HP: Distribution of the number of hits vs. z_{cog} for showers generated by a π^+ with a beam momentum of 3 GeV, **before** applying the cuts for hadron selection.

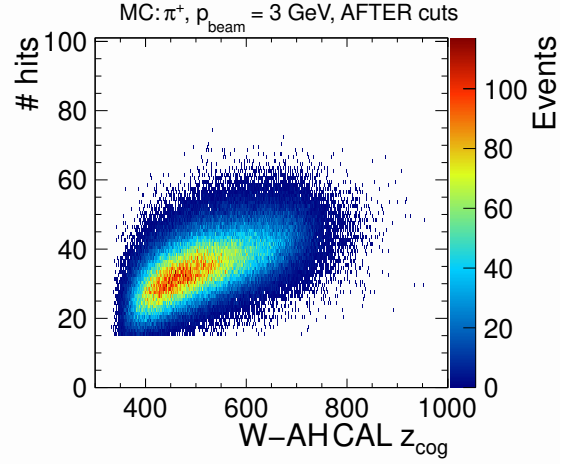


Figure 78: QGSP_BERT_HP: Distribution of the number of hits vs. z_{cog} for showers generated by a π^+ with a beam momentum of 3 GeV, **after** applying the cuts for hadron selection.

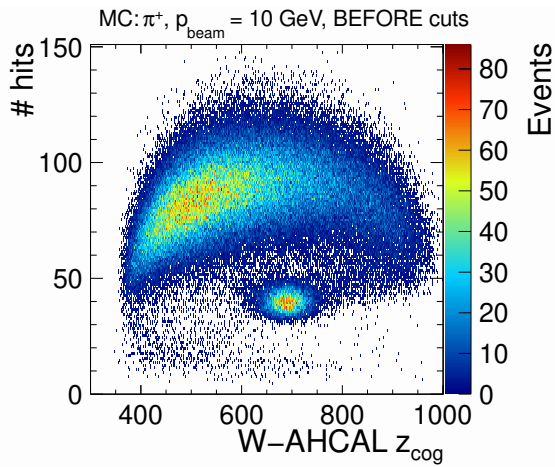


Figure 79: QGSP_BERT_HP: Distribution of the number of hits vs. z_{cog} for showers generated by a π^+ with a beam momentum of 10 GeV, **before** applying the cuts for hadron selection.

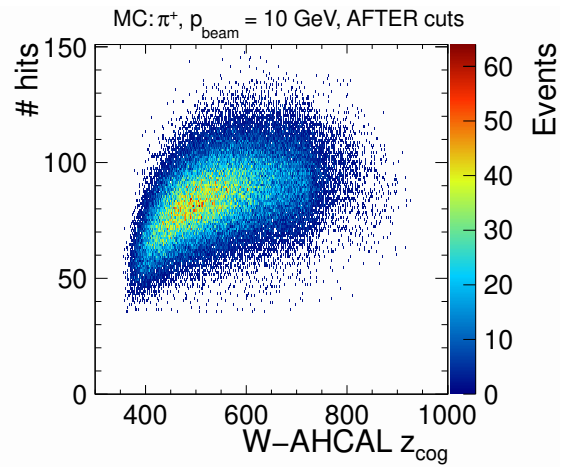


Figure 80: QGSP_BERT_HP: Distribution of the number of hits vs. z_{cog} for showers generated by a π^+ with a beam momentum of 10 GeV, **after** applying the cuts for hadron selection.

540 F. Comparison of methods to measure hadronic energy resolution

541 There are several methods to measure the hadronic energy resolution:

- 542 • In this analysis, we use Eq. 6.8, in order to take into account the tails observed in the visible
543 energy of low energy hadrons. This rather conservative method is labeled **RMS**.
- 544 • Another method is labeled **RMS90**, defined as in [29], i.e. similar to the above case, but
545 restricted to a region containing 90% of the statistics.
- A third method, more often used, labeled **Gauss fit**, is defined as:

$$\frac{\sigma_E}{E} = \frac{\sigma_{\text{Gauss}}}{\mu_{\text{Gauss}}}, \quad (\text{F.1})$$

546 where σ_{Gauss} is the width of the distribution obtained with a Gaussian fit in a limited region
547 (here we used a region containing 80% of the statistics, with respect to the mean of the
548 histogram), and μ_{Gauss} the corresponding mean from the fit.

549 The dependencies of the mean and widths of the distributions for the proton data, obtained
550 with the three methods, are presented in Figs. 81 and 82, and the corresponding energy resolutions
551 in Fig. 83. The methods do not change the conclusion about linearity (Table 21).

552 The energy resolution is fitted with the function given in Eq. 5.4. The Gaussian fits and the
553 RMS method are similar, the main difference consisting in the constant term, which is zero in the
554 first case, but with a large error. The RMS90 method clearly overestimates the energy resolution.
555 Therefore, when comparing the performance of different detectors, one has to consider carefully
556 which method is used for measuring the energy resolution.

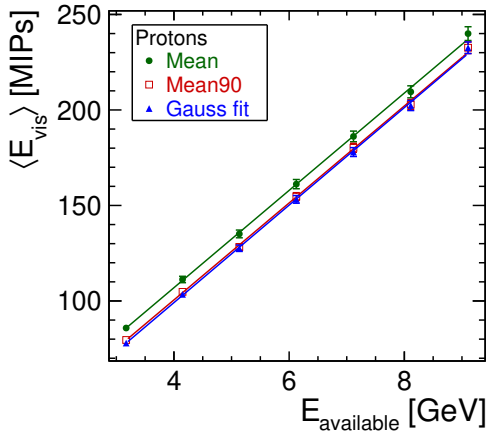


Figure 81: Dependence of the mean visible energy vs. the available energy for 2010 proton W-AHCAL data. The errors bars are given by the quadratic sum of the statistical and systematic errors. The lines indicate a fit with the function $\langle E_{\text{vis}} \rangle = u + v \cdot E_{\text{available}}$.

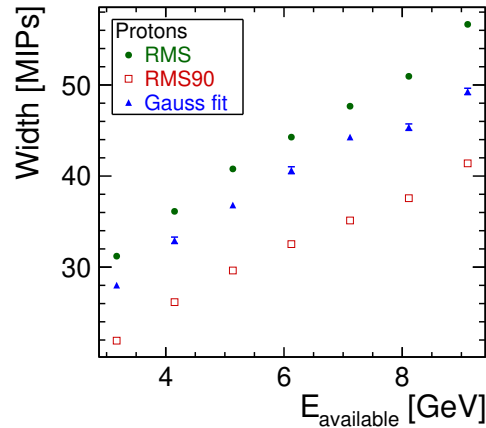


Figure 82: Dependence of the width of the mean visible energy vs. the available energy for 2010 proton W-AHCAL data. The errors bars are given by the quadratic sum of the statistical and systematic errors.

Parameter	Method		
	Mean	Mean90	Gauss fit
u [MIPs]	5.03 ± 2.24	-1.01 ± 1.83	-2.98 ± 1.82
v [MIPs/GeV]	25.48 ± 0.43	25.39 ± 0.36	25.53 ± 0.36
χ^2/ndf	1.4/5	1.9/5	1.8/5

Table 21: Fit parameters of the dependence of the mean proton visible energy on the available energy: comparison of methods.

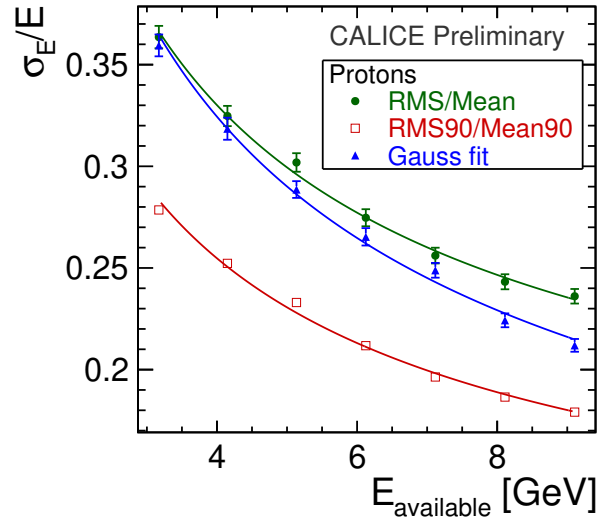


Figure 83: Proton resolution using different measurement methods.

557 **References**

- 558 [1] LCD study group, *Physics and Detectors at CLIC, Conceptual Design Report*, editors L. Linssen, A.
559 Miyamoto, M. Stanitzki and H. Weerts, CERN-2012-003
- 560 [2] C. Adloff *et al.*, *Construction and commissioning of the CALICE Analog Hadron Calorimeter*
561 *prototype*, JINST **5**, P05004 (2010), [arXiv:1003.2662 [physics.ins-det]]
- 562 [3] B. Bilki *et al.* *Hadron showers in a Digital Hadron Calorimeter*, JINST **4** (2009) P10008,
563 arXiv:0908.4236
- 564 [4] D. Dannheim, W. Klempt, E. van der Kraaij, *Beam tests with the CALICE tungsten analog hadronic*
565 *calorimeter prototype*, LCD-Note-2012-002
- 566 [5] CALICE collaboration, *Electromagnetic response of a highly granular hadronic calorimeter*, JINST **6**,
567 P04003 (2011), arXiv:1012.4343
- 568 [6] D. Dannheim, W. Klempt and A. Lucaci-Timoce, *Temperature studies of the CALICE W-HCAL with*
569 *CERN 2010 data*, LCD-Note-2011-001
- 570 [7] A. Lucaci-Timoce, *Analysis of W-AHCAL data*, talk given at the CALICE HCAL main meeting,
571 13 December 2011
- 572 [8] CALICE collaboration, *Local and global software compensation approaches: application to test beam*
573 *data*, CALICE Analysis Note CAN-035
- 574 [9] S. Richter, *Validation of the calibration procedure for a highly granular calorimeter with*
575 *electromagnetic processes*, diploma thesis, Hamburg Univ.
- 576 [10] L. Durieu, M. Martine and A.-S. Müller, *Optics studies for the T9 beam line in the CERN PS East*
577 *Area secondary beam facility*, Proceedings of the 2001 Particle Accelerator Conference, Chicago, 2001
- 578 [11] <http://sba.web.cern.ch/sba/BeamsAndAreas/East/East.htm>
- 579 [12] J. Spanggaard, *Delay Wire Chambers - A user's guide*, SL-Note-98-023, CERN, 1998
- 580 [13] CAEN Mod V1290 N, Technical information manual, 00104/03:V1X90.MUTx/11, 2010
- 581 [14] S. Agostinelly *et al.*, *GEANT4 – A simulation toolkit*, Nucl. Instrum. Meth. Phys. Res., Sect. A,
582 Vol. 506, pg. 250–303, 2003
- 583 [15] P. Mora de Freitas and H. Videau, *Detector simulation with MOKKA / GEANT4: Present and future*,
584 LC-TOOL-2003-010, prepared for International Workshop on Linear Colliders (LCWS 2002) Jeju
585 Island, Korea, 26-30 Aug 2002
- 586 [16] J. Apostolakis *et al.* *GEANT4 physics lists for HEP*, 2008 IEEE Nuclear Science Symposium
587 Conference Record, N02-89
- 588 [17] R. Wigman, *On the role of neutrons in hadron calorimetry*, Rev. Sci. Instrum. **69**, 3723 (1998)
- 589 [18] CALICE collaboration, *First T3B results - Initial study of the time of first hit in a*
590 *Scintillator-Tungsten HCAL*, CALICE Analysis note CAN-033
- 591 [19] Particle Data Group, *Review of particle physics*, J. Phys. G., **G37**, 075021 (2010)
- 592 [20] J. B. Birks, *The theory and practise of scintillation counting*, Macmillan, New York (1964).
- 593 [21] B. Lutz, *Hadron showers in a highly granular calorimeter*, PhD thesis, Hamburg Univ., 2010
- 594 [22] The RooFit toolkit for data modeling, <http://roofit.sourceforge.net/intro.html>

- 595 [23] BABAR collaboration, *Measurement of branching fraction and CP and isospin asymmetries for*
596 *$B \rightarrow K^* \gamma$* , Phys. Rev. **D70**, 112006 (2004)
- 597 [24] N. Feege, *Analysis of low-energetic electron and pion data collected with the AHCAL prototype at*
598 *Fermilab*, CALICE Analysis Note CAN-034
- 599 [25] CALICE collaboration, *DHCAL response to positrons and pions*, CALICE Analysis Note CAN-032
- 600 [26] L. Weuste, *Identification of track segments in hadronic showers in the Analog Hadron Calorimeter -*
601 *Algorithm and comparisons to simulations*, CALICE Analysis Note CAN-022
- 602 [27] P. de Barbaro, *Test beam performance of the CDF plug upgrade hadron calorimeter*, AIP Conf. Proc.
603 450, pp.405-413 (1997)
- 604 [28] N. Akchurin *et al.* *The response of CMS combined calorimeters to single hadrons, electrons and*
605 *muons*, CMS-NOTE-2007-012
- 606 [29] M.A. Thomson, *Particle Flow Calorimetry and the PandoraPFA Algorithm*, Nucl. Instrum. Meth.
607 **A611**:25-40 (2009), arXiv:0907.3577v1
- 608 [30] <http://root.cern.ch/root/html/TMath.html#TMath:Landau>